Published online 16 February 2023

Nucleic Acids Research, 2023, Vol. 51, No. 5 ***2215–2237***
https://doi.org/10.1093/nar/gkad066

PARP1 associates with R-loops to promote their resolution and genome stability

Natalie Laspata[1,2,†], Parminder Kaur[3,4,†], Sofiane Yacine Mersaoui[5,6,†], Daniela Muoio[1], Zhiyan Silvia Liu[7], Maxwell Henry Bannister[7], Hai Dang Nguyen[7], Caroline Curry[2], John M. Pascal[8], Guy G. Poirier[6,9], Hong Wang[3,4,10], Jean-Yves Masson[5,6] and Elise Fouquerel[1,*]

[1]UPMC Hillman Cancer Center, University of Pittsburgh Cancer Institute, Department of Pharmacology and Chemical Biology, Pittsburgh, PA 15213, USA, [2]Department of Biochemistry and Molecular Biology, Thomas Jefferson University, Philadelphia, PA 19107, USA, [3]Physics Department, Raleigh, NC 27695, USA, [4]Center for Human Health and the Environment, Raleigh, NC 27695, USA, [5]CHU de Québec Research Centre, HDQ Pavilion, Oncology Division, Laval University Cancer Research Center, McMahon, Québec City, Québec G1R 3S3, Canada, [6]Department of Molecular Biology, Medical Biochemistry and Pathology, Université Laval, Quebec, Canada, [7]Department of Pharmacology, The Masonic Cancer Center, University of Minnesota, Minneapolis, MN 55455, USA, [8]Department of Biochemistry and Molecular Medicine, Université de Montréal, Montréal, Québec H3C 3J7, Canada, [9]CHU de Québec Research Centre, CHUL Pavilion, Oncology Division, Quebec, Canada and [10]Toxicology Program, North Carolina State University, Raleigh, NC, USA

Received May 31, 2022; Revised January 19, 2023; Editorial Decision January 19, 2023; Accepted February 09, 2023

ABSTRACT

PARP1 is a DNA-dependent ADP-Ribose transferase with ADP-ribosylation activity that is triggered by DNA breaks and non-B DNA structures to mediate their resolution. PARP1 was also recently identified as a component of the R-loop-associated protein-protein interaction network, suggesting a potential role for PARP1 in resolving this structure. R-loops are three-stranded nucleic acid structures that consist of a RNA–DNA hybrid and a displaced non-template DNA strand. R-loops are involved in crucial physiological processes but can also be a source of genome instability if persistently unresolved. In this study, we demonstrate that PARP1 binds R-loops *in vitro* and associates with R-loop formation sites in cells which activates its ADP-ribosylation activity. Conversely, PARP1 inhibition or genetic depletion causes an accumulation of unresolved R-loops which promotes genomic instability. Our study reveals that PARP1 is a novel sensor for R-loops and highlights that PARP1 is a suppressor of R-loop-associated genomic instability.

GRAPHICAL ABSTRACT

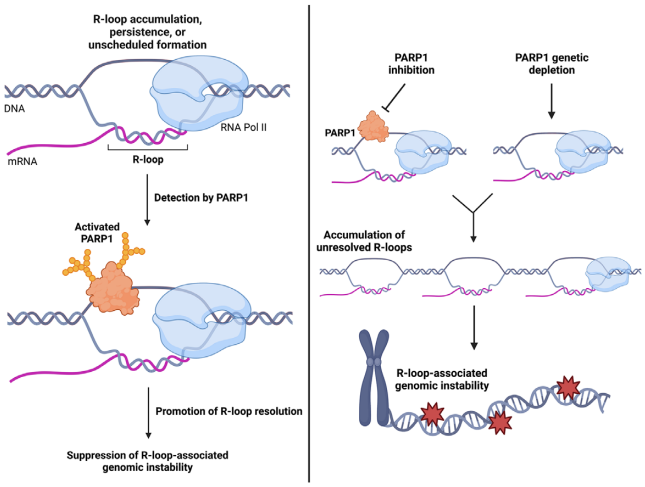

INTRODUCTION

PARP1 is a DNA-dependent ADP ribose transferase (ART) that utilizes NAD^+ to catalyze the transfer of ADP-ribose units onto itself, other protein targets and DNA ends (1–3). PARP1 catalytic activity enables the polymerization of up to 200 units of ADP-ribose leading to the synthesis of a branched poly(ADP-ribose) molecule (PARylation) (2). ADP-ribosylation is a posttranslational modification

*To whom correspondence should be addressed. Tel: +1 412 623 3237; Email: fouquerele3@upmc.edu; elf115@pitt.edu
†The authors wish it to be known that, in their opinion, the first three authors should be regarded as Joint First Authors.

of proteins that can modulate target protein interactions and recruitment dynamics in a given pathway. PARP1 has a broad DNA substrate specificity (4). Indeed, it has been found to bind to and be activated by single- and double-strand breaks (SSBs and DSBs), regardless of their end termini, and to DNA crosslinks, stalled replication forks, DNA hairpins, cruciform structures, G quadruplexes and even some RNAs and snoRNAs (4–11). Large-scale protein interaction network analysis revealed that PARP1 resides into complexes of R-loop-interacting proteins (12,13), suggesting a potential role for PARP1 in resolving this nucleic acid structure.

R-loops are three-stranded nucleic acid structures that consist of an RNA–DNA hybrid and a displaced non-template DNA strand. They mainly form co-transcriptionally during the promoter-proximal pausing of RNA polymerase II or when the nascent RNA invades the DNA duplex and re-anneals to the template strand, in a mechanism referred to as RNA 'thread-back' (14–18). The susceptibility for a genomic locus to form R-loops is determined by the negative supercoiling generated behind the RNA polymerase and by the DNA strand asymmetry in the cytosine and guanine content, a characteristic known as GC-skewing. During transcription of GC skews, the G-rich RNA strand will associate with the C-rich complementary DNA strand due to the superior thermodynamic stability of G-rich RNA:C-rich DNA hybrids (19). Therefore, hotspots for R-loop formation can be found at CpG island promoters, transcription termination regions and telomere TTAGGG repeats (20–22). There is also some evidence for forming of such structures in *trans*, especially at very short telomeres or during DSB repair processes (23–26).

R-loops play various physiological roles in several cellular processes such as class-switch recombination, transcription regulation, mitotic segregation, and epigenetic mechanisms (18–20,27–29). However, unwarranted formation, accumulation, or persistence of R-loops can threaten genomic stability in several ways, including mutagenesis and DNA lesions caused by replication-transcription collision or processing of unstable non-template DNA by various protein factors. Accordingly, unrestrained R-loop formation and accumulation are sources of increased genomic instability and chronic inflammation and are linked to several human neurodegenerative disorders and cancers (16,30,31). When present at telomeres, in particular, they have been found to cause telomere fragility and shortening and to be associated with telomerase-independent cancers (alternative lengthening of telomere (ALT) pathway) as well as immunodeficiency, centromeric instability and facial anomalies syndrome (ICF syndrome) (19,22,25,32–34).

Cells have developed various strategies and factors to regulate R-loop levels in the genome through their resolution or to prevent their formation directly. While the factors involved in nascent RNA surveillance and biogenesis can directly or indirectly prevent R-loop formation, the removal is mainly ensured by the ribonuclease enzyme RNase H that digests the RNA strand in the RNA–DNA hybrid, and several helicases such as Pif1, Senataxin (SETX) and many RNA–DNA helicases (12,17,19,34–38). Interestingly, a previous study reported an interaction between the DEAH-box helicase DHX9 and PARP1 and an enrichment of both proteins at the 3' end of the β-actin gene, corresponding to an R-loop-rich region and an increase of R-loop levels upon PARP1 depletion (12). More recently, a study revealed that PARP1 activity was found to promote the association of RNA helicase DDX18 with R-loops (39). Moreover, ATM-deficient cells were found to accumulate transcription-dependent R-loops and SSBs upon oxidative stress, leading to an activation of PARP1 and PARP2 that was abrogated following overexpression of SETX (40). Finally, depletion of the exoribonuclease XRN2, involved in R-loops resolution, triggered cell cytotoxicity in combination with PARP1 inhibition (41). While these studies strongly suggest a role for PARP1 in R-loop biology, whether PARP1 directly binds R-loops and is activated by its association with these structures, remains to be determined.

Herein, we provide evidence that PARP1 binds R-loop structures *in vitro* which triggers its enzymatic activity, using PARP binding activity assays and atomic force microscopy. We also show that PARP1 is recruited at R-loop formation sites in cells. Pharmacologic inhibition of PARP activity and genetic ablation of *PARP1* gene in cells increase the genomic R-loop level as evidenced by immuno-fluorescence and DRIP qPCR assays. Finally, lack of PARP1 or ADP-ribosylation activity enhances R-loop-mediated genomic instability. Our data strongly suggest a direct role for PARP1 in the detection and subsequent resolution of R-loop structures.

MATERIALS AND METHODS

Cell culture

To generate doxycycline-inducible U2OS cell lines expressing GFP-tagged wild-type or catalytically inactive RNase H1, ∼2.2 × 10^5 HEK293T cells (ATCC) were seeded in antibiotic-free growth media (DMEM + 10% iFBS) in a 6-well plate. The next day, the GFP-RNaseH1-M27 plasmids (500 ng) were used to co-transfect the cells with the VSV-G envelope (50 ng, Addgene #8454) and psPAX2 packaging (500 ng, Addgene #12260) plasmids in TransIT-LT1 transfection reagent (Mirus Bio #MIR2304) and OPTI-MEM reduced serum media (Gibco), and the cells were incubated overnight at 37°C and 5% O_2. The media was then replaced with 2.5 ml high BSA media (DMEM + 10% iFBS + 1 g/100 ml BSA + 1× pen-strep (Gibco)), and the cells were incubated for 24 h. In parallel, U2OS host cells were seeded in antibiotic growth media (DMEM + 10% FBS + 1× pen-strep) in a 6-well plate to be 70–80% confluent at the time of infection. The next day, lentivirus particles from the HEK293T cells were harvested and filtered through 0.2 μm filters. The U2OS host cells were transduced with a 1:1 ratio of lentivirus to media containing polybrene (Millipore #TR-1003-G) at 1:1000 concentration and incubated overnight. The following day, the infection was repeated with the remaining lentiviral harvest. Cells were allowed to recover for 8–10 h in standard growth media before being selected for G418 resistance in selection media for 1–2 days (DMEM + 10% FBS + 1× pen-strep + 500 μg/ml G418). Bulk populations were treated with doxycycline (DOX; 1 μg/ml, Fisher Scientific #BP26531) for

24 h to induce RNase H1 expression, diluted to a density of 5×10^6 cells/ml, and individual GFP-positive cells were sorted into 96-well plates using a BD FACSMelody™ cell sorter. Each expanded clone was seeded in glass-bottom 35 mm dishes and then induced with DOX for 24 h. The next day, the cells were fixed for 10 min on ice in 2% formaldehyde in PBS (PFA) and then tested for RNH1-GFP expression using a Nikon Eclipse Ti2-E microscope. Clones were also tested for RNH1-GFP expression by western blot with a standard SDS-PAGE gel (NuPAGE 4–12% Bis-Tris, ThermoFisher Scientific) using anti-GFP (GeneTex #GTX20290; 1:1000 concentration) and anti-β-actin (Clone AC15, Sigma-Aldrich #A1978; 1:50,000 concentration) antibodies after 24 h of DOX treatment. Following single-cell cloning, cells were cultured in specialized media for the tetracycline-inducible system (DMEM + 10% TET-system approved FBS (Gibco) + 1× pen-strep + 500 μg/ml G418).

U2OS PARP1ko cells were obtained as previously described (39). RNH1-inducible PARP1ko cells were obtained by infection of U2OS RNH1-GFP cells with lentivirus expressing *S. pyogenes* Cas9 (SpCas9) and a guide RNA targeting *PARP1* exon 2 (gRNA 6, sequence GTGGCCCACCTTCCAGAAGC). Guide RNAs were designed and validated to specifically target the human PARP1 gene by the laboratory of Feng Zhang at the Broad Institute (Sanjana et al., 2014) and were incorporated into pLentiCRISPRv2 vectors (GenScript). For lentiviral production, HEK293T cells were seeded in a 6-well plate and the next day, 500 ng of pLentiCRISPRv2-PARP1 plasmid was co-transfected with the VSV-G (50 ng) and psPAX2 (500 ng) plasmids in TransIT-LT reagent and OPTI-MEM. U2OS RNH1-GFP cells were transduced twice over two days with a 1:1 lentiviral harvest to media with polybrene. Cells were selected for puromycin resistance in selection media for 1–2 days (DMEM + 10% TET-FBS + 1× pen-strep + 1.5 μg/ml puromycin (Gibco)). Knockout efficiency was validated in the bulk cell population by western blot using PARP1 monoclonal (C-2–10, Enzo #BML-SA250-0050; 1:1000 concentration) and anti-β-actin antibodies. Single-cell cloning was then performed to generate a stable PARP1ko cell line. 400 cells from the bulk population were seeded in a 150 mm dish, ensuring proper spreading, and the cells were allowed to grow for 2 weeks or until colonies were visible with the naked eye. Colonies were carefully transferred into 96-well plates by trypsinization within an open-ended glass cloning cylinder (Corning) dipped in high vacuum grease (Dow Corning) and pressed against the bottom of the dish. Each expanded clone was tested for PARP1 expression by western blot with the C-2–10 antibody.

For PARP1 complementation experiments, U2OS RNH1-GFP cells were seeded in 100 mm dishes in G418 media (DMEM + 10% TET-FBS + 1× pen-strep + 500 μg/ml G418) so that they were 70–90% confluent at the time of transfection. The pCMV-PARP1-3XFLAG plasmid (5 μg) was used to transfect the cells with FuGENE HD transfection reagent (Promega #E2311) in OPTI-MEM and the cells were incubated overnight. The next day, the media was replaced with fresh G418 containing media and the cells were allowed to recover for 24 h. PARP1 expression was validated by western blot using anti-PARP1 (C-2–10), anti-DDDDK (FLAG) tag (Abcam #ab1162; 1:4000 concentration), and anti-β-actin antibodies.

For siRNA knockdown experiments, Dharmacon™ ON-TARGETplus SMARTPool siRNA for human Senataxin (SETX) and PARP1 were purchased from Horizon (PARP1 #L-006656-03-0005, SETX #L-021420-00-0005). Silencer® Select siRNAs for RNase H1 were purchased from Invitrogen (#s48357 (siRNA57) and #s48358 (siRNA58)). For SETX and RNH1 knockdowns, U2OS cells were seeded in 60 mm dishes in standard growth media (DMEM + 10% FBS + 1× pen-strep) so that they were 70–80% confluent at the time of transfection. Each siRNA was used to transfect the cells overnight at 50 nM concentration in serum-free DMEM and DharmaFECT 1 transfection reagent (Horizon #T-2001-02) after a 30 min incubation at RT, during which the cell media was replaced with antibiotic-free DMEM + 10% FBS. The next day, the media was replaced with standard growth media and the cells were allowed to recover for 24 h. Knockdown efficiency for RNH1 siRNA was validated by western blot on a standard SDS-PAGE gel using the anti-RNase H1 (H-4, Santa Cruz Biotechnology #sc-376326) and anti-β-actin antibodies. To validate SETX siRNA efficiency, western blot was performed with a NuPAGE 3–8% Tris-acetate gel (ThermoFisher Scientific) using the anti-SETX (Bethyl Laboratories #A301-104A) and anti-β-actin antibodies. For PARP1 knockdown, RNH1-GFP cells were seeded in 100 mm dishes in TET-FBS media. The siRNA transfection was performed as done for RNH1 and SETX, scaling up to accommodate the dish size. Knockdown efficiency was validated by western blot using the anti-PARP1 C-2–10 and anti-tubulin antibodies.

The HeLa cell lines expressing GFP-RNaseH1-WT-M27 or GFP-RNaseH1-D210N-M27 cells were obtained as previously described (42). A Cas9 sgRNA targeting exon 2 of the *PARP1* gene (sgPARP1-1, 5'-CAGCAGAATTCCCCGATCCG-3') was cloned into lentiCRISPRv2 (Addgene #52961) and transformed into Stbl3 competent cells. The lentiCRISPRv2-sgPARP1-1 (10 μg) was packaged into lentiviral particles by co-transfecting the packaging plasmids pCMV-VSV-G (10 μg, Addgene #8454) and pCMV-dR8.2 dVPR (10 μg, Addgene #8455) into HEK293T cells. Viral particles were collected, infected into HeLa expressing inducible GFP-RNaseH1-WT-M27 cells and selected using puromycin.

Recombinant PARP1 preparation

Human PARP1 was expressed in *Escherichia coli* using expression vector pET28 (Novagen) with an N-terminal hexahistidine tag and was purified using three chromatography steps: Ni(II)-affinity, heparin, and gel filtration (43). AFM assays were performed using recombinant human PARP1 purchased from Trevigen.

pFC53-m*AIRN* plasmid purification

R-loop substrates were generated using the pFC53-m*AIRN* plasmid, a gift from Dr Sara Selig (Israel Institute of Technology), which forms R-loop when transcribed with T3 RNA polymerase *in vitro.* Plasmid preparation included a

cesium chloride purification prior to IVT to remove any nicked or linear plasmid DNA and to enrich supercoiled plasmid. Plasmid was digested with the unique cutter enzyme HindIII before and after IVT to verify that the linear plasmid had the predicted size. Plasmid DNA was diluted in 1× TE buffer (Fisher Scientific) to a volume of 2.5 ml, weighed on a sensitive scale, and 1.01 g of CsCl (Fisher Scientific) per 1 g of DNA/TE mixture was added. A blank sample was made by weighing 5 ml of 1× TE buffer and adding 1.01 g CsCl per 1 g of TE, and this blank was used to bring the DNA samples up to a final volume of 4.75 ml, which was then transferred into a polypropylene centrifuge tube (Beckman Coulter #362185). Each uncapped centrifuge tube, along with its respective cap, was weighed to ensure that the difference in mass between them was as close to zero as possible. The tubes, caps, centrifuge rotor (Beckman Coulter VTi 65.2), and EtBr (ThermoFisher Scientific #15585011) were taken into a darkroom and 140 μl of EtBr was carefully added to each tube. The contents of the tubes were gently mixed with a pipette before being placed inside the rotor and then the bolts were tightened to at least 140 psi. The samples were centrifuged at 20°C for 16 h at 45 000 rpm. The next day, the tubes were retrieved from the rotor and the band corresponding to the supercoiled plasmid DNA was carefully extracted, in the dark, by puncturing one side of the tube with an 18-gauge beveled needle (BD Biosciences #305185) attached to a 3 ml syringe (BD Biosciences #309657). The DNA was transferred into 15 ml conical tubes wrapped in aluminum foil and the EtBr was removed with 6–7 additions of 2 ml H_2O-saturated 1-butanol (2:3 ratio of H_2O to butanol) by removing the aqueous phase until it became clear. The DNA samples were then transferred into 3 ml dialysis cassettes (ThermoFisher Scientific #87728), and CsCl was removed by floating the cassettes in 1× TE with gentle stirring for 1 h at RT and then in fresh TE overnight at 4°C. The following day, the DNA samples were transferred into Eppendorf tubes and either stored at -80°C or precipitated with 100% ethanol and 3M sodium acetate, pH 5.2.

In vitro transcription (IVT) for R-loop formation with the pFC53-*mAIRN* plasmid

Reactions were prepared by combining 3 μg pFC53-m*AIRN,* 1× transcription optimized buffer (Promega #P1181; 40 mM Tris (pH 7.9), 6 mM $MgCl_2$, 2 mM spermidine, 10 mM NaCl) supplemented with 20 mM DTT, 0.05% Tween-20, and 0.25 mM rNTP mix on ice. Transcription was initiated by adding 160 U of T3 RNA polymerase (Promega #P4024). Samples were incubated at 37°C for 30 min and heat-inactivated at 65°C for 10 min. To remove free RNAs, samples were treated with 0.01 mg/ml RNase A (Thermo Scientific #EN0531) at 37°C for 30 min. 10 U of *E. coli* RNase H (ecRNH; NEB #M0297L) were added to negative control samples and incubated at 37°C for 30 min to destroy RNA–DNA hybrid structures. 60 U of RNase T1 (ThermoScientific #EN0541) was also used to degrade free RNAs. To verify the presence of R-loop structures, 200 ng of each sample was run on a 0.9% agarose, 1× TBE gel at 100V for 1 to 1.5 h and post-stained with EtBr. The gel was imaged using a GE Healthcare Amersham Imager 600.

Purification and ethanol precipitation of R-loop substrates

After gel verification of R-loop formation, substrates were purified by adding one volume of phenol:chloroform:isoamyl alcohol (25:24:1, v/v, Invitrogen #15593049) and centrifuging in phase lock gel heavy centrifuge tubes (Quanta Bio #2302830). DNA was precipitated from the aqueous phase by adding 2.5 volumes of 100% ethanol, 0.1 volumes of 3M sodium acetate pH 5.2, and incubating at –20°C overnight. The next day, DNA was pelleted by centrifugation, washed with 70% ethanol, air dried, and resuspended in 1× TE buffer. Sample concentration was then obtained using a DeNovix DS-11 spectrophotometer.

PARP1 auto-modification assays

For assays performed using R-loop substrates generated in the pFC53-m*AIRN* plasmid, samples were prepared by combining 1× PARP1 activity buffer, 125 nM purified PARP1 protein, and 125 nM purified DNase I-activated DNA (for positive control, Enzo #ALX-840–040-C010) or purified pFC53-m*AIRN* plasmid DNA (either un-transcribed or transcribed). Samples were incubated at 22°C for 10 min, 2.5 μM NAD^+ (Enzo #BML-KI282-0500) was added, and the samples were incubated for another 5 min at 22°C. An equal volume of 2× Laemmli sample buffer (Bio Rad #1610737EDU) with 0.1M EDTA was added, samples were boiled at 95°C for 5 min and run on a 10% polyacrylamide SDS-PAGE gel at 80–120V for ∼1.5 h. The gel was stained with Coomassie brilliant blue in a mixture of 50% methanol, 10% acetic acid, and 40% H_2O for 1 hr at RT and de-stained in the same mixture without Coomassie for 1 h at RT. The gel was imaged using a GE Healthcare Amersham Imager 600.

For the anti-PAR western blot analyses, a PARP1 auto-modification assay was first performed as described above, followed by transfer onto nitrocellulose membrane (instead of staining with Coomassie) at 25 V for 1.5 h at RT. The membrane was blocked in 5% milk in TBS-Tween (TBS-T) and incubated with the mouse anti-PAR 10H antibody (Enzo #ALX-804-220-R100) at 1:1000 concentration overnight at 4°C. The next day, the membrane was incubated with a goat anti-mouse secondary antibody at 1:5000 concentration for 1 hr at RT and developed with ECL detection reagents (Amersham/Cytiva). The gels used to obtain the data of Figures 2B and C were imaged using a GE Healthcare Amersham Imager 600. The gels used to obtain the data of Figures 2A, I and J were imaged using a Biorad Gel Doc XR imager. Band signal intensities were quantified using ImageJ software. for each substrate we set background with the 'noNAD' sample. The signal intensity values obtained in the 'noNAD' sample was subtracted from the '+NAD' sample. Then the 'noDNA' sample was set as a baseline (= 1; not displayed on the graphics) for all the other samples to calculate the fold increase.

Electrophoretic mobility shift assays

For PARP1 EMSA using DNA fragments (related to Supplementary Figure 1C and D), reactions were performed in buffer containing 25 mM MOPS pH 7.0, 60 mM KCl, 0.2%

Tween-20, 2 mM DTT, 5 mM $MgCl_2$, 10% glycerol with 100 nM ^{32}P-labeled oligonucleotides and purified PARP-1 at the indicated concentrations (0–50 nM). The reaction mixtures were incubated at 37°C for 15 min followed by fixation with 0.2% glutaraldehyde, and then another incubation for 15 min at 37°C. DNA samples were loaded onto 8% native polyacrylamide gel and products were separated by electrophoresis in 1× TBE buffer. The gel was dried using a vacuum gel dryer (Bio-Rad) for 35 min at 85°C, then revealed using Fujifilm FLA 5100. The DNA substrates were generated by annealing and purification on native polyacrylamide gels. The oligonucleotides used were:

ssDNA: JYM3702 (5′GGGTGAACCTGCAGGTGGGCGGCTGCTCATCGTAGGTTAGTTGGTAGAATTCGGCAGCGTC3′)

dsDNA: JYM3702 + JYM3703 (5′GACGCTGCCGAATTCTACCAGTGCCTTGCTAGGACATCTTTGCCCACCTGCAGGTTCACCC3′)

Loop: JYM3702 + JYM4358 (5′GGGTGAACCTGCAGGTGGGC*AAAGATGTCCTAGCAAGGCACTGG*AGAATTCGGCAGCGTC3′)

D-Loop: JYM3702 + JYM3703 + JYM3705 (AAAGATGTCCTAGCAAGGCAC)

R-loop: JYM3702 + JYM3703 + JYM3704 (AAAGAUGUCCUAGCAAGGCAC)

RNA–DNA hybrid: JYM3702 + JYM4358 + JYM3704

ssRNA: JYM3704

dsRNA: JYM3701 + JYM4638 (GUGCCUUGCUAGGACAUCUUU)

For PARP1 EMSAs using the pFC53-m*AIRN* plasmid (related to Supplementary Figure 1E), reactions were prepared by combining 172 nM purified PARP1 protein, 1× PARP1 activity buffer (500 mM Tris–HCl pH 8.0, 40 mM $MgCl_2$, 2 mM DTT, 500 μg/ml BSA), and 200 ng pFC53-m*AIRN* plasmid (either un-transcribed for control condition or transcribed for experimental condition). Samples were incubated at RT for 10 mins and run on a 0.5% agarose gel in 0.5× TBE and post-stained with SYBR™ Safe DNA Gel Stain (Invitrogen #S33102). The gel was imaged using a GE Healthcare Amersham Imager 600.

For S9.6 and BG4 antibody EMSAs, reactions were prepared by combining 200 ng pFC53-m*AIRN* plasmid DNA (either un-transcribed or transcribed), 1× PARP1 activity buffer, and 1.4 pmol of primary antibody, either S9.6 to bind R-loop structures or BG4 (Sigma-Aldrich #MABE917) to detect G-quadruplex structures. Samples were incubated at RT for 10 min and run on a 0.5% agarose gel in 0.5× TBE and post-stained with SYBR™ Safe DNA Gel Stain. The gel was imaged using a GE Healthcare Amersham Imager 600.

Atomic force microscopy imaging and image analysis

R-loop substrates were generated through *in vitro* transcription using pFC53-*mAIRN* as described above. The circular DNA with R-loops and control DNA were linearized using ApaLI overnight to generate two linear DNA fragments and purified using the Zymo DNA purification kit (44). Purified linear pFC53-*mAIRN* DNA with or without R-loops (3 nM) was incubated with PARP1 (Trevigen, 50 nM) at 37°C in PARP1 Binding Buffer (50 mM Tris–HCl pH 8.0, 10 mM $MgCl_2$ 1 mM DTT, 12.5 mM NaCl) for 10 min. For activating PARP1, purified linear pFC53-*mAIRN* DNA with or without R-loops (3 nM) was incubated with PARP1 (50 nM) in PARP1 Activation Buffer (50 mM Tris–HCl, pH 8.0, 10 mM $MgCl_2$, 1 mM DTT, 0.3 mM NAD^+ and 12.5 mM NaCl) at 37°C or on ice, for 1 min and 10 min, respectively. The reaction mixtures were diluted 16-fold in Imaging Buffer (20 mM HEPES, pH 7.5, 100 mM NaCl, 10 mM $Mg(OAc)_2$) and immediately deposited onto a freshly cleaved mica surface (SPI). The samples were then washed with MilliQ water and dried under a stream of N_2 gas. All images were collected using the AC mode on an MFP-3D-Bio AFM (Asylum Research) using PPP-FMR probes (Nanosensors, Spring constant (*k*: ∼2.8 N/m). The images were captured at a scan size of 1–3 μm × 1–3 μm at a resolution of 512 × 512–1024 × 1024 pixels and a scan rate of 1 Hz. Ample time is given for the AFM system to reach thermal equilibrium to avoid any distortion in AFM images due to thermal drift. AFM samples were scanned at a low scan rate (1 Hz), and the feedback parameters were also adjusted to obtain identical forward and backward profiles in the cross-section analysis. To minimize the compression of the sample, AFM imaging was operated with soft approach (low set point forces and/or low drive amplitudes) so that the AFM tips exerts only minimum force on the samples.

The positions of PARP1 and activated PARP1 on DNA were analyzed using software from Asylum Research. For images of PARP1 binding to DNA containing R-loops, the threshold for selecting molecules was set at 1 nm height.

RNA–DNA hybrid immunodetection by slot blot

Slot blot experiments were conducted as described previously in (45). Briefly, nucleic acids were extracted from U2OS cells by SDS and proteinase K treatment at 37°C overnight, followed by phenol-chloroform extraction and ethanol precipitation. After nucleic acid quantification using a NanoDrop™, 1 μg of extract was diluted or not as indicated and blotted onto Hybond-N nylon membrane in duplicate using a slot blot apparatus (Schleicher & Schuell). One half of the membrane was treated with 0.5 N NaOH and 1.5 M NaCl for 10 min to denature the DNA and neutralized for another 10 min in 0.5 M Tris–HCl buffer (pH 7.0) containing 1 M NaCl. After UV-cross-linking (0.12 J/m^2), the non-treated membrane was subjected to western blot analysis with S9.6, and the treated membrane, served as loading control, with the single-stranded DNA antibody (Clone 16–19, Millipore MAB3034). The S9.6 signal was normalized by the loading control.

For S9.6 dot blot experiments with siRNA knockdown, cells were harvested from 60 mm dishes approximately 48 h after transfection. For S9.6 dot blot in PARP1 complementation experiment, cells were harvested 72 h after transfection with the plasmid coding for the CRISPR insensitive flag-tagged PARP1. Genomic DNA was extracted using the Qiagen Blood & Cell Culture DNA Mini Kit (#13323) following manufacturer instructions for Preparation of Cell Culture Samples (pages 25–30 of QIAGEN Genomic DNA Handbook) and then for Isolation of Genomic DNA from Cultured Cells using Genomic-tip 20/G (pages 49–52 of handbook). Genomic DNA concentration

was quantified using a NanoDrop™ One Microvolume UV-Vis Spectrophotometer (ThermoFisher Scientific). RNase H treatment was performed with 5 U of ecRNH (NEB) and incubated at 37°C for 30 min. All samples were then brought up to a final volume of 200 μl with 2× saline-sodium citrate (SSC; Fisher Scientific) and spotted onto a Hybond-N membrane in duplicate using a Minifold I dot blot apparatus (Schleicher & Schuell). One half of the membrane (for the ssDNA control) was denatured and then neutralized for 10 min each at RT before being crosslinked, blocked for 1 h at RT in 5% milk, and incubated overnight in the anti-ssDNA antibody at 1:250 concentration. The other half of the membrane (for S9.6 detection) was directly crosslinked after dot-blotting, blocked in 5% milk, and incubated overnight with the S9.6 antibody at 1:1000 concentration. The membranes were developed using ECL detection reagents and images were acquired, and signals quantified, using a Biorad Gel Doc XR imager and software. Fold changes compare to U2OS cells were determined after determination of ssDNA volumes used as loading controls.

Sub-cellular fractionation and quantification of chromatin-bound PARP1

2×10^6 cells were seeded in 6-well plates. The following day, cells were treated with 0.4 μg/ml of DOX along with 100nM of Talazoparib for 24 h. Cells were then collected following trypsin treatment, resuspended in 1ml of media and counted using the automated Invitrogen Countess cell counter. The subcellular fractionation was performed using the Subcellular Protein Fractionation Kit (ThermoFisher Scientific #78840) according to manufacturer instructions. Buffer volumes were adapted according to the number of cells counted. The chromatin-bound nuclear extracts were then resolved on NuPAGE 4–12% Bis–Tris mini protein gel and transfered onto nitrocellulose membrane for the subsequent incubation with anti-PARP1 C-2–10 (Enzo #BML-SA250-0050) and anti-Histone H3 (1B1-B2, Novus Biologicals #BP2-36468) antibodies. Western blot band volumes were determine using the BioRad Image Lab software. For each experiment, Histone H3 signals were used as loading controls and PARP1 volumes detected in DOX-only-treated cells were set as the basal levels of chromatin-bound PARP1.

Immunofluorescence

RNA–DNA hybrid immuno-detection was conducted as described in (46). Briefly, coverslips containing U2OS-cells were fixed with 2 ml of ice-cold, 100% methanol for 10 min at –20°C. Coverslips and cells were then washed once with PBS before subsequent steps. Coverslips were then incubated in staining buffer (TBS-T + 0.1% BSA) for 10 min with rocking. Enzymatic treatments were done in staining buffer supplemented with 3 mM $MgCl_2$ with 1:200 dilutions of RNase T1 (EN0541; Thermo Fisher Scientific), ShortCut RNase III (M0245S; New England Biolabs), and/or ecRNH and incubated for 1 h at 37°C. Coverslips were subsequently washed by incubating with staining buffer for 10 min with rocking at RT. For primary immunolabeling, coverslips were incubated in staining buffer with 1:1000 dilutions of the mouse S9.6 (purified from the HB-8730 hybridoma cell line), and 1:1000 dilutions of a rabbit anti-nucleolin antibody (Abcam #ab50279) from Abcam. Primary antibodies were incubated for a minimum of 1h at room temperature with rocking. Coverslips were then washed once with staining buffer and incubated with 1:1000 dilutions of secondary anti-mouse Alexa Fluor® 488 conjugate (Invitrogen Life Technologies #A11001) and anti-rabbit Alexa Fluor® 568 conjugate (Invitrogen Life Technologies #A11011) in the same manner as for the primary antibody incubation, with samples protected from light from this step onward. Alexa Fluor-conjugated goat anti-rabbit antibodies and anti-mouse antibodies were from Invitrogen (Carlsbad, CA). After rinsing with TBS-T for 10 min, coverslips were mounted with Immuno-Mount (Thermo Scientific) mounting medium containing 1 μg/ml of 4',6-diamidino-2phenylindole (DAPI). Images were acquired at 63x magnification on a Leica DMI6000 (Figure 4) or Nikon Eclipse Ti2-E microscope.

The RNA–DNA hybrid staining in HeLa cells was processed as previously described (42) (H.D.N lab). HeLa cells were trypsinized, pelleted and resuspended in hypotonic solution (75 mM KCl) prewarmed to 37°C while being agitated on a vortex at a low speed. Then cells were incubated at 37°C for 12 min before adding 5–6 drops of freshly made, ice-cold fixation solution (methanol/glacial acetic acid 3:1 ratio). Cells were pelleted at 1000 rpm for 5 min, and supernatant was aspirated down to 500 μl. 6 ml of the fixation solution was added to the cells in a drop-wise manner while cells being agitated on a vortex at a low speed. Cells were fixed for 20 min and washed one more time with the fixation solution before being spread on a coverslip. Dried slides were blocked with blocking buffer (1× PBS, 5% BSA, 0.5% Triton X-100) for 1 h at room temperature and S9.6 antibody (purified from the HB-8730 hybridoma cell line, 1 μg/μl, 1:500) was incubated overnight at 4°C. The slides were washed three times with the wash buffer (1× PBS + 0.1% Triton X-100) and subsequently incubated with mouse secondary antibody conjugated with Cy3 for 1 h at room temperature. Cells were washed three times with the wash buffer and then stained with DAPI and mounted using ProLong™ Gold Antifade Mountant (Invitrogen).

For G4 immuno-fluorescence, cells were treated with DOX as previously or pyridostatin (PDS) at 10 μM concentration for 24 h. The next day, cells were washed 2 times with ice-cold 1× PBS and incubated for 2 min in cytoskeletal extraction buffer (CSK; 10 mM PIPES, 100 mM NaCl, 300 mM sucrose, 2 mM $MgCl_2$, 0.25% Triton-X100, 1 mM DTT) on ice. Cells were then fixed for 10 min on ice in 2% PFA, permeabilized in 1× PBS + 0.5% Triton-X100 for 10 min at RT, blocked in Blocking Buffer (1× PBS + 10% normal goat serum + 1% BSA) for 1 hr at RT, and incubated with a BG4-FLAG primary antibody (Millipore #MABE917) diluted in blocking buffer at 1:500 concentration overnight at 4°C. The following day, cells were incubated with an anti-FLAG antibody (Abcam #ab1162) at 1:1000 for 1 h at 37°C and then with an Alexa Fluor® 647 goat anti-rabbit antibody diluted in blocking buffer at 1:1000 concentration for 1 h at RT. Cells were mounted with ProLong™ Gold Antifade Mountant with DAPI.

For γH2AX immuno-detection, U2OS cells were seeded on 22 mm coverslips in 6-well plates in specialized media (DMEM + 10% TET-system approved FBS + 1× pen-strep + 500 μg/ml G418). Prior to fixation, cells were labeled with EdU from the Click-iT™ EdU Cell Proliferation Kit for Imaging, Alexa Fluor® 647 dye (Invitrogen #C10340) according to manufacturer protocol. Cells were fixed on ice in 2% PFA in 1× PBS, permeabilized in 1× PBS + 0.5% Triton-X100 for 10 mins at RT, blocked in blocking buffer (1× PBS + 10% normal goat serum + 1% BSA) for 1 hour at room temperature, and incubated with γH2AX primary antibody (Abcam #ab11174) diluted in blocking buffer at 1:500 concentration overnight at 4°C. The following day, cells were incubated with an Alexa Fluor® 594 goat-anti-rabbit antibody diluted in blocking buffer at 1:1000 concentration for 1 hour at room temperature. EdU detection was performed with Click-iT™ kit after γH2AX immunofluorescence staining, using Click-iT™ EdU cell proliferation kit for imaging, Alexa Fluor 647 (Invitrogen #C10340) following manufacturer protocol. Cells were rinsed in PBS and H2O prior to mounting in ProLong™ Gold Antifade Mountant with DAPI (Invitrogen #P36931).

For PAR10H immuno-fluorescence experiments, cells were seeded on coverslips in 6-well plates in specialized media to be ∼70% confluent the next day, when 10 μM PARG inhibitor PDD00017273 and 0.4 μg/ml DOX were added and incubated for 24 h. The following day, cells were fixed in a 1:1 mixture of ice-cold methanol:acetone on ice for 10 mins, followed by fixation in 2% PFA in 1× PBS on ice for 10 min, permeabilization in 1× PBS + 0.5% Triton-X100 for 10 min, and blocking in blocking buffer for 1 h at RT. Coverslips were incubated over night with the mouse anti-PAR 10H primary antibody diluted in blocking buffer at 1:1000 concentration and then with an Alexa Fluor® 594 goat anti-mouse antibody at 1:1000 concentration for 1 h the next day before being mounted with ProLong™ Gold Antifade Mountant with DAPI (Invitrogen #P36931). All images were acquired using the Nikon Eclipse Ti2-E microscope and deconvolved using NIS Elements software.

Proximity ligation assays (PLA)

PLA experiments were performed using the DuoLink® In Situ Red Starter Kit Mouse/Rabbit (Millipore/Sigma-Aldrich #DUO92101-1KT) and following manufacturer protocol with modifications. Cells were seeded on 18 × 18 mm glass coverslips in a 6-well plate and treated with 0.4 μg/ml DOX for 24 h. For S9.6/PARP1 PLA, cells were treated with fresh cytoskeletal pre-extraction buffer (CSK; 10 mM PIPES, 100 mM NaCl, 300 mM sucrose, 2 mM $MgCl_2$, 0.25% Triton-X100, 1 mM DTT) for 2 mins on ice, fixed in 2% PFA in 1× PBS for 10 min on ice, permeabilized in 1× PBS + 0.5% Triton-X100 for 10 min at RT, blocked in blocking buffer for 1 hr at RT, and incubated with S9.6 (1:1000 concentration) and PARP1 (1:1000) rabbit primary antibodies (Enzo #ALX-210-302-R100) diluted in blocking buffer overnight at 4°C. Alternatively, cells were processed following the RNA–DNA hybrid immunofluorescence protocol as described above to include the RNases T1, III and ecRNH controls. The PLA assay was performed the next day according to manufacturer protocol beginning from Step 3. Following final washes, coverslips were mounted with ProLong™ Gold Antifade Mountant with DAPI. Images were obtained using the Nikon® Eclipse Ti2-E microscope.

For the G4:PARP1 PLA, we followed the G4 immunofluorescence protocol described above prior to PLA staining. Because the FLAG tag antibody used in our experiment is a rabbit antibody, we used the mouse PARP1 C-2–10 antibody (Enzo #BML-SA250-0050). For each experiment, antibody controls were performed in which one antibody was incubated without the other. In the case of G4:PARP1 PLA, the following controls were included: BG4 only, PARP1 only, BG4 + FLAG, BG4 + PARP1 (no FLAG).

Population doubling (PD)

1.10×10^5 RNH1-D210N-GFP U2OS cells were seeded in 6-well plates. The next day, the cells were induced with 0.4 μg/ml DOX and incubated for 2, 4 or 6 days, with one well of the 6-well plate being harvested and counted at each timepoint. Cells were counted using a Countess automated cell counter (Invitrogen). Data and statistical analyses were performed using Graphpad Prism 9 software.

MTT assay

5000, 7500 or 10 000 D210N-RNH1-GFP U2OS cells were seeded in triplicate in 96-well plates. The next day, cells were induced with 0.4 μg/ml DOX and incubated for 24 h. MTT assay was then performed using the Abcam MTT Assay Kit (Cell Proliferation; #ab211091) following manufacturer protocol. Data and statistical analyses were performed using Graphpad Prism 9 software.

DRIP-qPCR

DRIP assays were performed as described in (47). Briefly, DNA containing R-loops was extracted from U2OS cells by SDS/proteinase K treatment at 37°C overnight, followed by phenol-chloroform extraction using MaXtractTM High Density (100 × 15 ml from QIAGEN) and ethanol precipitation at RT. The harvested DNA was digested for 24 h at 37°C using a restriction enzyme cocktail (50 units/100 μg nucleic acids, each of BsrGI, EcoRI, HindIII, SspI, and XbaI) in the CutSmart buffer (New England Biolabs) with 2 mM Spermidine and 1× BSA. Digested DNAs were cleaned up by phenol–chloroform extraction using MaXtractTM High Density (200 × 2 ml) followed by treatment or not with ecRNH (20 units/100 μg nucleic acids) overnight at 37°C in ecRNH buffer (New England Biolabs). RNA–DNA hybrids from 4.4 μg digested nucleic acids, treated or not with ecRNH, were immunoprecipitated using 10 μg of S9.6 antibody (purified from the HB-8730 hybridoma cell line) and 50 μl of protein A/G agarose beads (Sigma-Aldrich) at 4°C for 2 h or overnight in IP buffer (10 mM $NaPO_4$, 140 mM NaCl and 0.05% Triton X-100). The beads were then washed four times with IP buffer for 10 min at RT, and the nucleic acids were eluted with elution buffer (50 mM Tris–HCl, pH 8.0, 10 mM EDTA, 0.5% SDS and 70 μg of protease K) at 55°C for 1 hr. Immunoprecipitated

DNA was then cleaned up by a phenol–chloroform extraction followed by EtOH precipitation with 20 μg glycogen at 20°C for 1 h. The enriched chromatin was analyzed by qPCR using the following primers:

JYM5602 (Actin RB-F: CAACTGGGACGACATGGAGAAA),
JYM5603 (Actin RB-R: GAGTCCTACGGAAAACGGCAGA),
JYM5604 (Actin PA-F: TGTACACTGACTTGAGACCAGT),
JYM5605 (Actin PA-R: AAGCAGGAACAGAGACCTGACC),
JYM5606 (Actin RD-F: TAGGCTTAGGAGAGGCCGCAAT),
JYM5607 Actin RD-R: GTCCAGGAGCCTGGGTATCTCC),
JYM5203 (Egr1-F: TTCGGATTCCCGCAGTGT),
JYM5204 (Egr1-R: TCACTTTCCCCCCTTTATCCA),
FOS-F: CCTGCAAGATCCCTGATGACCT),
FOS-R: AGGGTGAAGGCCTCCTCAGACT),
JYM5124 (RPL13A-F: AGGTGCCTTGCTCACAGAGT),
JYM5125 (RPL13A-R: GGTTGCATTGCCCTCATTAC),
EGR1 Downstream-F: (GAACGTTCAGCCTCGTTCTC),
EGR1 Downstream-R: (GGAAGGTGGAAGGAAACACA).

Reverse transcription and real-time quantitative PCR (RT–qPCR) analysis

Total cellular RNA was isolated from siRNA-transfected U2OS cells using RNeasy Mini Kit (Qiagen) according to the manufacturer's instructions. cDNA was synthetized using ProtoScript® II First Strand cDNA Synthesis Kit containing M-MLV Reverse Transcription with randomized Primer Mix. The cDNA were analyzed by real-time quantitative PCR (RT–PCR) using SYBR Green PCR Master Mix (Applied Biosystems). The primers used: HPRT, B2M and RPPO were used as housekeeping gene expression for normalization.

JYM5433 (RPP0-F: TTCATTGTGGGAGCAGAC),
JYM5434 (RPP0-R: CAGCAGTTTCTCCAGAGC),
JYM4915 (HPRT1-F: CCTGGCGTCGTGATTAGTGA),
JYM4916 (HPRT1-R: TCTCGAGCAAGACGTTCAGT),
JYM4913 (B2M-F: TGGGTTTCATCCATCCGACA),
JYM4914 (B2M-R: ATGCGGCATCTTCAAACCTC),
b-Actin-F: CATGTACGTTGCTATCCAGGC,
b-Actin-R: CTCCTTAATGTCACGCACGAT,
EGR1-F: GGTCAGTGGCCTAGTGAGC,
EGR1-R: GTGCCGCTGAGTAAATGGGA.

Microscopy imaging analyses

For images requiring the quantification of foci (γH2AX and PLA), the Nikon NIS Element software was used. The quantification process included the isolation of individual nuclei as regions of interest (ROI) using the DAPI channel. The intensity threshold tool was used to select the foci in the appropriate channel (Cy3 for the PLA and γH2AX foci). This threshold was maintained for all images within the same replicate experiment. The foci were then qualified as 'objects' and automatically quantified by the software for each ROI selected. The data were exported into Microsoft Excel and then imported into GraphPad Prism 9 for graphing and for statistical analyses.

The nuclei were selected as described above for images requiring the quantification of overall fluorescence signal intensity (PAR 10H, GFP and S9.6 signals). The resulting ROIs were exported as 'new binary layers,' and the intensity of the signal underneath the ROIs was collected for each channel, exported into Excel and then copied into GraphPad Prism 9 for graphing and statical analyses.

RESULTS

PARP1 associates with R-loops *in vitro*

To test whether R-loops are a substrate for PARP1, we interrogated the direct binding of PARP1 to R-loop structures *in vitro*. We purified recombinant PARP1 and validated that it was active by PARP1 auto-modification assay using DNase1-activated DNA (aDNA) and NAD^+. PARP1 auto-modification by poly(ADP-ribose) prevents the protein from entering the gel, which is depicted by a decrease of Coomassie band intensity at the PARP1 molecular weight level (Supplementary Figure 1A and B).

We first tested the binding affinity of PARP1 by electrophoretic mobility shift assay (EMSA) without NAD^+ to prevent PARP1 release from the DNA. We prepared radioactive 61mer ssDNA, 61 bp dsDNA, RNA–DNA hybrids, dsDNA containing a loop (Loop) as well as D-loop and R-loop substrates for which integrity was verified by gel electrophoresis (Supplementary Figure 1C). Importantly, the faster migration of both paired RNA–DNA hybrid and R-loop substrates upon digestion with E.coli RNaseH enzyme (ecRNH), which digests the RNA moiety within a hybrid, confirmed the presence of the RNA (Supplementary Figure 1C, right panel). EMSA assays and determination of affinity binding curves and constants (KD) revealed that, in our experimental conditions, PARP1 had the highest affinity for ssDNA and the lowest affinity for a paired RNA–DNA hybrids (Supplementary Figures 1D and 1E; Supplementary Table 1). We also noted a significant increase of PARP1 affinity for R-loops when compared to the hybrids, suggesting that the displaced ssDNA of the R-loop may contribute to the recognition of the structure by PARP1. It is also noteworthy that regardless of the DNA end similarity between the D-loop and the R-loop substrates, PARP1 seemed to bind with more affinity to the R-loops indicating a role for the RNA component. However, we did not observe binding of PARP1 to the 22-mer ssRNA and dsRNA (Supplementary Figure 1F) suggesting that the hybrid component is one of the keys to PARP1 binding to this complex structure rather than the RNA itself. The absence of PARP1 binding to the 22-mer RNA substrates is in line with previous studies demonstrating poor binding of PARP1 to short RNAs (11). Overall, this assay confirms the high affinity of PARP1 for a variety of DNA substrates, notably DNA ends as previously shown (4,48), but also brings evidence for PARP1 binding to R-loop structures.

We next performed atomic force microscopy (AFM) to directly visualize the binding of PARP1 to R-loops. To do this, we generated R-loop structures using a plasmid containing the mouse gene mAIRN (pFC-mAIRN) (Figure 1A). The mouse gene *AIRN* is a CpG island that harbors oriented GC skews downstream of a T3 promoter that is prone to R-loop formation upon *in vitro* transcription (IVT) with the T3 RNA polymerase (20,49) (Figure 1A). The plasmid was purified by cesium chloride (Supplementary Figure 1G) and digested with the unique cutter HindIII to confirm that it had the predicted size (Supplementary Figure 1J). Digestion with ExoIII, an exonuclease that initiates at nicked sites present in dsDNA and digests the DNA strand that carries the nicks, confirmed the absence of nicked molecules after cesium chloride purification (Supplementary Figure 1H). The formation of R-loops upon IVT was confirmed by the slower migration of the R-loop-containing plasmid molecules on an agarose gel (Figure 1B). The slower migration was not abolished upon RNase A treatment, which only degrades the free RNAs synthesized during the IVT process. However, a treatment with the ecRNH restored the initial electrophoretic mobility of pFC-*mAIRN*, thereby indicating that RNA–DNA hybrid formation is responsible for the electrophoretic mobility change of the plasmid (Figure 1B). To further confirm the formation of the R-loops, we performed an EMSA assay using the RNA–DNA hybrid antibody S9.6 that was demonstrated to bind RNA–DNA hybrids without binding dsDNA *in vitro* (50). While incubation of the S9.6 antibody with non-transcribed plasmid molecules (pFC-mAIRN) did not yield any band shift (Figure 1C; compare lane 1 with lane 2), we observed a band-shift with *in vitro* transcribed plasmid molecules (pFC-mAIRN/RL) after their incubation with the S9.6 antibody (Figure 1C; compare lane 3 with lane 4), confirming the presence of RNA–DNA hybrids in the structure.

As expected, the EMSA assay with PARP1 yielded band shifts for both pFC-mAIRN and pFC-mAIRN/RL (Supplementary Figure 1I), due to PARP1's affinity for dsDNA. Therefore, to further localize PARP1 on pFC-mAIRN and pFC-mAIRN/RL substrates, we utilized AFM imaging that allows for the visualization of proteins on DNA substrates at the single-molecule level (51–53). To facilitate imaging, the pFC-mAIRN plasmid was digested with the restriction enzyme ApaL1 after IVT to generate a short (1246 bp) and a long (2745 bp) linear DNA fragment (Figure 1A; Supplementary Figure 1J). Upon IVT, we confirmed that the 2745 bp-long fragment harbored the expected R-loops, as illustrated by its slower migration on the agarose gel (Supplementary Figure 1J, compare lane 2 with lane 4).

After ensuring digestion of the plasmid molecules by ApaL1, the DNA fragments were incubated in PARP1 assay buffer with PARP1 for 10 min at room temperature without NAD^+ and deposited on the mica surface for AFM imaging. We utilized the distinct lengths of the DNA fragments in the AFM images (short: 375.1 ± 21.9 nm; long: 787.6 ± 34.6 nm; mean ± SD) to distinguish the short fragments that does not harbor the R-loops from the long DNA fragments harboring the R-loops. The mouse AIRN gene was previously shown to form R-loops at two different G-rich sites (49) located at 38% and 42% from the closest DNA end of the 2745 bp fragment (49,52). In agreement with these previous reports (49,52), we observed different R-loop shapes at this location, including blobs (40%), spurs (32%), and loops (28%) (Figure 1D). In addition, R-loops displayed significantly greater average height (0.82 ± 0.08 nm) (Figure 1G) than dsDNA (0.34 ± 0.09 nm; data not shown) and were positioned at 40.8 ± 5% from the closest DNA end on the long DNA fragment (Figure 1H).

Next, to investigate whether PARP1 directly binds to R-loops, we incubated PARP1 with the DNA fragments *in vitro,* either transcribed or not (without NAD^+) for 10 min at room temperature and deposited them on the mica surface. Imaging of DNA molecules with PARP1 revealed protein-DNA complexes with heights averaging 1.01 ± 0.40 nm (Supplementary Figure 1K) that were greater than dsDNA and R-loops alone, thereby validating the presence of PARP1 on DNA. Additionally, regardless of the presence of R-loops in the dsDNA fragments, we observed the presence of PARP1 at DNA ends (0% from the closest end), as anticipated due to its strong affinity for DNA ends (4) (Figure 1H). When PARP1 was incubated with the dsDNA fragments generated from the un-transcribed plasmid, we observed a random distribution of PARP1 along the dsDNA (28.40 ± 13.30%) (Figures 1E and H), thereby confirming the moderate affinity of PARP1 for undamaged DNA previously documented (54,55). However, upon incubation of PARP1 with dsDNA fragments generated from the transcribed plasmid, we noted an enrichment of complexes with a height distribution higher than PARP1 on un-transcribed dsDNA (1.38 ± 0.56 nm) (Figure 1G; Supplementary Figure 1L) at 35.00 ± 11.10% from the closest DNA end, corresponding to the R-loop containing region (Figures 1F and H). In order to verify that the *in vitro* transcription (IVT) and purification processes did not introduce modifications in the DNA substrate that would mediate unspecific PARP1 binding, we also tested the binding of PARP1 on dsDNA fragments generated from plasmid that underwent a 'mock' IVT. Consistent with what we reported with fragments from un-transcribed plasmid, PARP1 binding occurred preferentially at the DNA ends as well as randomly along the dsDNA (Supplementary Figure 1M). Taken together, our data demonstrate that PARP1 can associate preferentially with R-loop structures *in vitro*.

PARP1 association with R-loops triggers its ADP-ribosylation activity

PARP1 binding to its DNA substrates is responsible for activating its ADP-ribosylation activity (5). We therefore asked whether its binding to an R-loop leads to PAR synthesis. To test this, we performed *in vitro* PARP1 automodification assays. We incubated PARP1 with the pFC-mAIRN and pFC-mAIRN/RL substrates in the PARP1 activity buffer. DNase I-activated DNA (aDNA) was used as a positive control and a sample without DNA was added as a negative control.

First, we verified that the purification process used to obtain pure pFC-mAIRN/RL substrate following IVT (see Methods section for details) did not generate any DNA structures that could potentially activate PARP1 activity independently of the presence of an R-loop. We subjected a

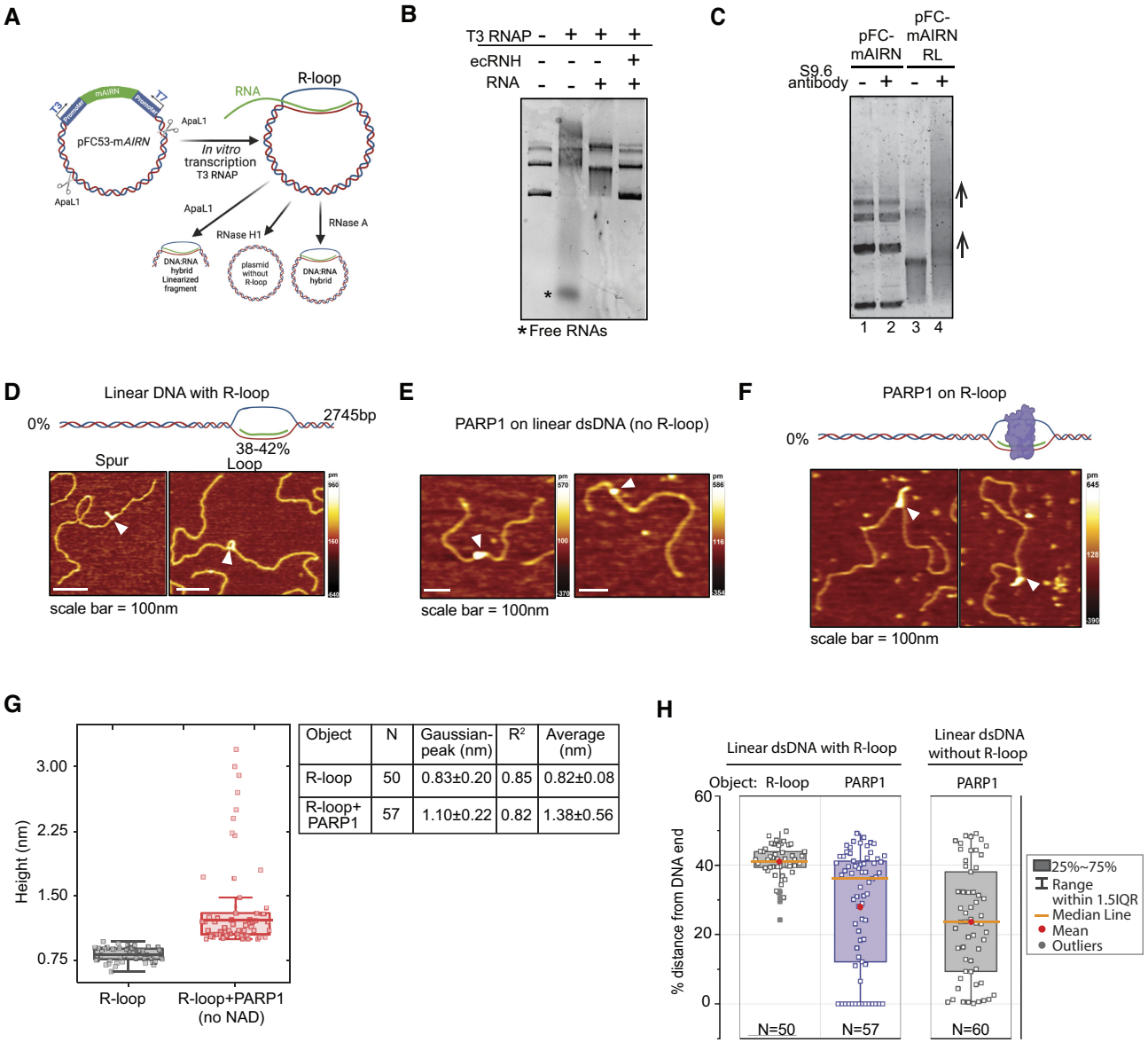

Object	N	Gaussian-peak (nm)	R^2	Average (nm)
R-loop	50	0.83±0.20	0.85	0.82±0.08
R-loop+ PARP1	57	1.10±0.22	0.82	1.38±0.56

Figure 1. PARP1 associates with R-loops *in vitro*. (**A**) Generation of R-loop-containing substrates for *in vitro* studies using the pFC53-m*AIRN* plasmid. For AFM studies, T3 RNAP-transcribed plasmid was linearized with ApaLI to yield an R-loop-containing fragment. For downstream biochemical experiments, transcribed plasmid was treated with RNase A to degrade residual RNAs while preserving R-loop structures. A negative control was generated by treatment of transcribed plasmid with E. coli RNase H (ecRNH) to degrade R-loops. (**B**) Agarose gel electrophoresis verifying R-loop formation in the pFC-m*AIRN* plasmid following T3 IVT. Migration of un-transcribed plasmid (lane 1), transcribed plasmid (lane 2), transcribed plasmid treated with RNase A (lane 3), and transcribed plasmid treated with RNase A and ecRNH (lane 4) was analyzed. R-loop formation in the transcribed plasmid is indicated by a shift in migration. ecRNH treatment degrades R-loops and abrogates this shift. (**C**) EMSA assay of un-transcribed (lanes 1 and 2) or transcribed pFC-m*AIRN* plasmid fragments (lanes 3 and 4) incubated with the R-loop antibody S9.6 (lanes 2 and 4). Black arrows indicate the super-shift caused by S9.6 binding to R-loops. (**D**) AFM topography images of transcribed, linear 2795 bp pFC-m*AIRN* plasmid fragments containing R-loops (right panel, white arrow) and spurs (left panel, white arrow) without PARP1. (**E**) AFM topography images of un-transcribed, linear 2795 bp pFC-m*AIRN* plasmid fragments (no R-loops) incubated with PARP1 (white arrows depict PARP1 binding). (**F**) AFM topography images of transcribed, linear 2795 bp pFC-m*AIRN* plasmid containing R-loops incubated with PARP1 (white arrows depict PARP1 binding). Examples are from samples incubated at RT for 10 min. XY scale bar = 100 nm. (**G**) AFM height distribution of R-loops on the linear DNA fragments without PARP1 (0.82 nm ± 0.08 nm, $N = 50$) versus inactive PARP1 bound to R-loops on the linear DNA (1.38 nm ± 0.56 nm, $N = 57$). Numbers reported: Mean ± SD. (**H**) Position distribution of R-loops on the linear DNA fragments without PARP1 (40.8% ± 5.0%, $N = 50$), PARP1 on the linear DNA with R-loops (+R-loop, 35.0% ± 11.1% not counting end binding, $N = 55$) and PARP1 on linear DNA without R-loops (-R-loop, 28.4% ± 13.3% not counting end binding, $N = 47$). Numbers reported: Mean ± SD. The Box–Whisker plots show 25–75%, median, mean and range within 1.5 IQR.

plasmid sample to mock IVT in which all components of the IVT reaction were added except for the rNTPs. The mock IVT plasmid molecules (pFC-mAIRN/mock) were then treated with RNase A for degradation of free RNAs and purified by phenol-chloroform extraction and ethanol precipitation, similarly to pFC-mAIRN/RL DNA substrates. We then incubated 125 nM of pFC-mAIRN or 125 nM of pFC-mAIRN/mock with PARP1 and NAD^+, along with no DNA and aDNA controls, and assessed PARP1 activity by anti-PAR western blot (Figure 2A). We observed a robust PARP1 activation upon incubation with aDNA, as expected. PARP1 incubation with pFC-mAIRN also triggered PARylation above background (noDNA) but we did not observe any increase of PAR signal in the sample containing pFC-mAIRN/mock when compared to the noDNA sample. This data indicates that the R-loop purification process does not impact PARP1 activity and can be included in our assays.

We next set out to test whether the presence of an R-loop in the pFC-mAIRN plasmid (pFC-mAIRN/RL) was sufficient to trigger PARylation *in vitro*. We compared PAR synthesis upon PARP1 auto-modification in samples containing noDNA or 125 nM of aDNA, pFC-mAIRN and pFC-mAIRN/RL. We quantified the PAR signal intensity obtained by western blot and estimated the fold increase over the noDNA control, which we set as the background PAR level (lane 2; Figures 2B and C). We also quantified the related Coomassie-stained PARP1 signals on SDS-PAGE gels by setting the background signal in the noDNA and no NAD^+ sample (lane 1; Supplementary Figures 2A and 2B). As expected, PARP1 auto-modification was robustly triggered in the presence of aDNA and NAD^+ as illustrated by the decrease of PARP1 signal on the Coomassie stained gel and the detection of a high molecular weight PAR smear by western blot (lanes 1 to 4; Supplementary Figure 2A and B; Figure 2B and C; Supplementary Table 2). The addition of pFC-m*AIRN* DNA without R-loop slightly triggered PAR synthesis (lanes 5–6; Figure 2A–C; Supplementary Figure 2A and B). Most importantly, PARP1 activity was increased when incubated with pFC-mAIRN/RL when compared to the non-transcribed pFC-m*AIRN* DNA (lanes 7 and 8; Figure 2A–C; Supplementary Figure 2A and B). Finally, we also treated transcribed pFC-mAIRN plasmid with the ecRNH1, or with RNase T1 (RNT1), an exoribonuclease that degrades single stranded RNAs only (ssRNAs) while preserving intact R-loop-containing substrates as illustrated by agarose gel electrophoresis (Supplementary Figure 2C). While treatment with RNT1 did not alter PARylation, treatment with ecRNH, prevented PARP1 activation (Supplementary Figure 2D). Taken together, the PARP1 auto-modification assays indicate that PARP1 is activated by the R-loops harbored by the plasmid molecules.

We then interrogated the location of activated PARP1 molecules on R-loop-containing dsDNA fragments by AFM imaging. We first used the same incubation parameters described above: PARP1 was incubated with NAD^+ and dsDNA fragments generated from the transcribed plasmid in the PARP1 assay buffer for 10 min at room temperature prior to the deposition of the protein/DNA complexes onto the mica surface for AFM imaging. However, in these conditions, we noted a strong PARP1 activity that led to the formation of aggregates that prevented the evaluation of PARP1 binding and activation at the individual molecule level (Supplementary Figure 2E). Conversely, when the different components were incubated for 10 min on ice or 1 min at 37°C, we could collect single protein/DNA molecules. We confirmed that under these special conditions, inactivated PARP1 could still bind similarly to what we observed previously (Compare Supplementary Figure 2F with Figure 1H; 35.3 ± 7.5 distance from closest DNA end for $t_{incubation} = 10$ min on ice and 33.03 ± 13.1% distance from closest DNA end for $t_{incubation} = 1$ min at 37°C). When NAD^+ was incubated with PARP1, we noted complexes showing proteins harboring additional branched chains that were absent in the samples without NAD^+ which we attributed to PAR polymers (Figure 2D). These complexes had greater height distribution than inactivated PARP1 on R-loop-containing DNA (Compare Figure 2E with 1H). Importantly, activated PARP1 molecules with branched chains were specifically located at the regions corresponding to R-loop regions (35.00 ± 9.70%, $N = 36$, for $t_{incubation} = 10$ min on ice; 32.40 ± 12.66%, $N = 21$, $t_{incubation} = 1$ min at 37°C) (Figures 2F), demonstrating a preference of activated PARP1 for R-loops. In summary, both the bulk biochemical assays and AFM imaging demonstrated that PARP1 association with R-loops triggers its activity.

PARP1 association with R-loops triggers bridging at R-loop sites

During our observation of our AFM slides, we also detected the formation of complexes containing multiple DNA molecules bound to PARP1 (15.7% DNA molecules; Figure 2G). To locate the site of bridging, we measured the length of the DNA strand short arms from the closest end to the junction point. While R-loops could be found at 314.00 ± 38.70 nm from the end, the short arm length measured in these multi-DNA complexes averaged 301.60 ± 79.50 nm, indicating that PARP1 activation promoted bridging at R-loop sites (Figure 2H).

PARP1 association with R-loops is not mediated by the formation of G4 structures in the displaced ssDNA

R-loops are prevalent at GC-rich loci due to enhanced stability between the C-rich DNA and the G-rich RNA of the hybrid (49,56). Thus, R-loops formation can correlate with the appearance of G quadruplexes (G4s) within the displaced G-rich non-template DNA (57,58). PARP1 has been described to bind to and be activated by G4 structures *in vitro* and *in cellulo* (6–9). Thus, we verified whether PARP1 binding to R-loops *in vitro* could be mediated by G4 formation within the displaced DNA strand. The mAIRN locus is a CpG island with high G content in the non-template DNA that is predicted to form G4s when transcribed in the physiological orientation (T3 RNAP; Supplementary Figure 2G). However, the probability of G4 formation drops significantly when mAIRN is transcribed in the anti-physiological orientation (T7 RNAP; Supplementary Figure 2G), which can be accomplished using the T7 promoter harbored by the pFC-mAIRN plasmid, downstream of the *mAIRN* coding sequence (Figure 1A). We therefore performed IVT using the T7 RNAP. The formation of R-loops

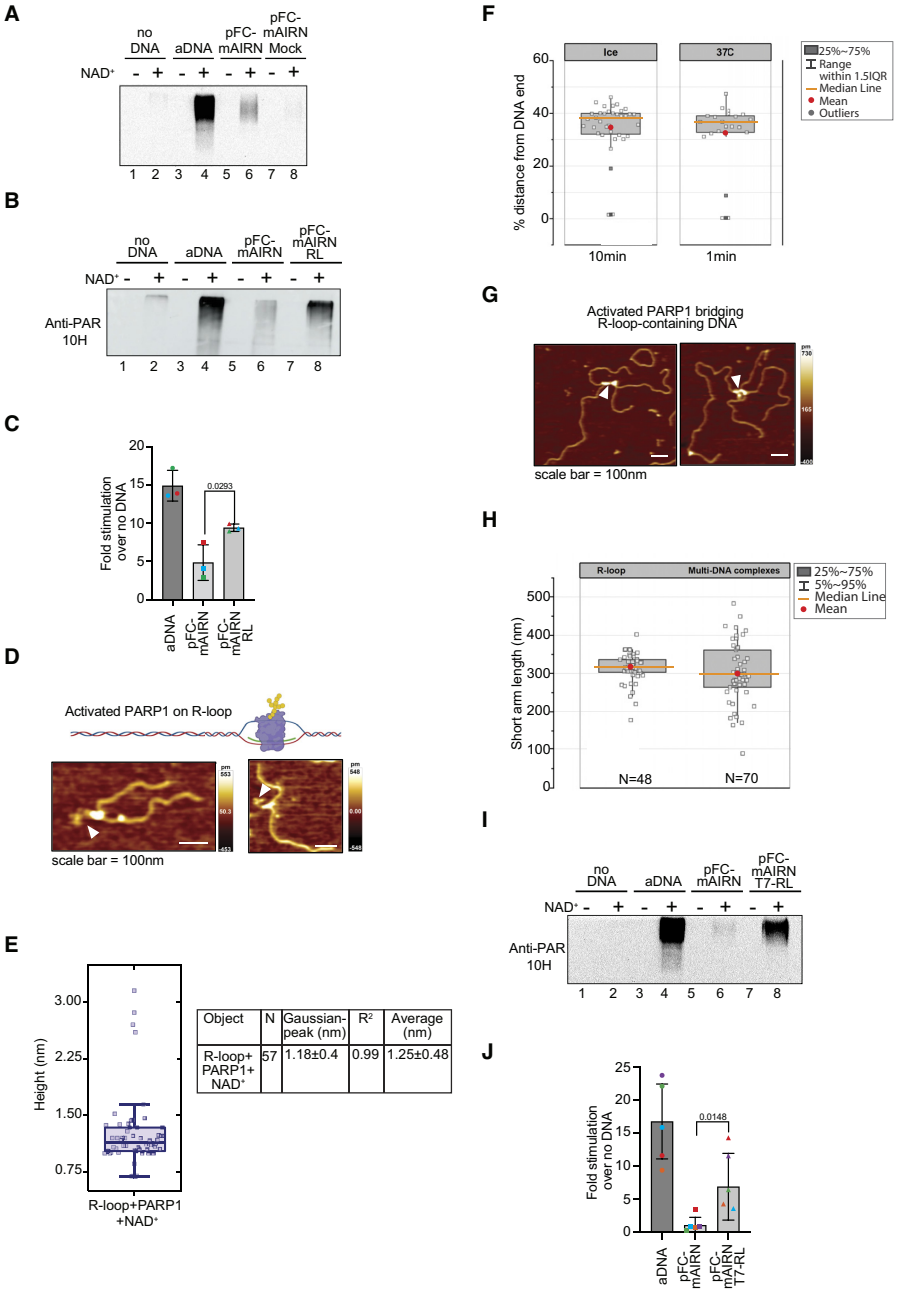

Figure 2. PARP1 association with R-loops triggers ADP-ribosylation activity. (**A**) Anti-PAR 10H western blot following PARP1 auto-modification assay demonstrating that the IVT process does not induce modifications in pFC-m*AIRN* DNA that mediate unspecific PARP1 binding, indicated by a lack of increase in PAR signal when PARP1 is incubated with plasmid that underwent the mock IVT process compared to the no DNA control. DNase I-activated DNA (aDNA) fragments were used as a positive control for PARP1 activation. A sample without DNA (no DNA) was used as a negative control. (**B**) Anti-PAR 10H western blot following PARP1 auto-modification assay demonstrating activation of purified PARP1 upon incubation with un-transcribed or T3 RNAP-transcribed pFC-m*AIRN* plasmid.(**C**) Quantification of fold stimulation of PARP1 activity over no DNA control observed by anti-PAR western blot illustrated in (B). Data are from 3 independent experiments, indicated by colored data points. *P* value was obtained using an unpaired student's t-test assuming 95% confidence. (**D**) Representative AFM topography images of a linear, transcribed 2795 bp pFC-m*AIRN* fragment containing R-loops incubated with activated PARP1. White arrows indicate PAR branched chains on PARP1. XY scale bar = 100 nm. (**E**) AFM height distribution of linear, transcribed pFC-m*AIRN* molecules containing R-loops incubated with activated PARP1. (**F**) Position distribution of activated PARP1 on linear, transcribed pFC-m*AIRN* fragments containing R-loops (position distribution on ice = 35.0% ± 9.7%, $N = 36$; position distribution at 37°C = 32.4% ± 12.6%, $N = 21$). Numbers reported: mean ± SD. The Box–Whisker plots show 25–75%, median, mean, and range within 1.5 IQR. (**G**) AFM topography images of PARP1 bridging transcribed pFC-m*AIRN* fragments at R-loop sites. XY scale bar = 100 nm. (**H**) Measurement of short arm length of the bridged pFC-m*AIRN* molecules in (G) from the closest end to the junction point. Short arm length$_{\text{R-loop}}$ = 314 ± 38.7 nm, short arm length$_{\text{multi-DNA complex}}$ = 301.6 ± 79.5 nm, $N = 50$, $P > 0.05$) Numbers reported: mean ± SD. The Box–Whisker plots show 25–75%, 5–95%, median, and mean. (**I**) Anti-PAR western blot following PARP1 auto-modification assay demonstrating activation of purified PARP1 upon incubation with un-transcribed or T7-transcribed pFC-m*AIRN* DNA. (**J**) Quantification of fold stimulation of PARP1 activity over no DNA control observed by anti-PAR western blot illustrated in (I). Data are from five independent experiments, identified by colored data points. *P* values was obtained using an unpaired Student's *t*-test assuming 95% confidence.

was confirmed by a band shift, which was prevented upon ecRNH treatment (Supplementary Figure 2H). The plasmid molecules obtained after T7 IVT (pFC-mAIRN/T7-RL) were then tested in a PARP auto-modification assay along with pFC-mAIRN plasmid or aDNA and noDNA controls. Like previously, we confirmed a robust PARP1 activation upon incubation with aDNA and NAD^+ and a light activation upon incubation with pFC-mAIRN (Figure 2I and J; Supplementary Table 1). Importantly, incubation of PARP1 with NAD^+ and pFC-mAIRN/T7-RL also led to an increase of auto-PARylation compared to non-transcribed plasmids (Figure 2I and J). This data suggests that PARP1 association to R-loop and its subsequent activation is not mediated solely by potential formation of G4 structures within the displaced DNA.

PARP1 associates with R-loop-forming sites in cells

PARP1 has already been reported in the R-loop protein interactome (12). However, its association with R-loop-forming sites in cells has not yet been tested. Because our biochemical assays reveal a direct association of the enzyme with R-loops, we next asked whether PARP1 is localized at R-loop-forming sites in cells. We established stable U2OS cell lines from clones in which the expression of GFP-tagged wild-type or the catalytically inactive human RNase H1 enzyme (RNH1-WT-GFP and RNH1-D210N-GFP, respectively) is driven by a tetracycline-inducible promoter. Accordingly, treatment of these cells with doxycycline for 24 h induced RNH1-WT-GFP and RNH1-D210N-GFP expression, detected by fluorescence microscopy and western blot using a GFP-specific antibody (Supplementary Figures 3A and 3B). The RNH1-D210N-GFP mutant can recognize and bind to RNA–DNA hybrids but, unlike the wild-type enzyme, cannot cleave the RNA moiety within the hybrid. Its over expression slows down R-loop resolution in cells and increases R-loop stability and basal levels. RNase H1 was shown to fulfill other functions distinct from R-loop resolution, such as mitochondrial DNA replication (59,60). It was also suggested to play a role in the removal of RNA primers of the RNA–DNA hybrids in Okazaki fragments (61–63). Because of these other functions, we verified that the overexpression of both RNH1-WT-GFP and RNH1-D210N-GFP did not impact cell growth, replication, and cell viability. The measurement of population doubling (PD) times of cells treated with doxycycline during a period of 6 days indicated that overexpression of RNH1-WT-GFP and RNH1-D210N-GFP did not significantly impact overall cell growth (Supplementary Figure 3C). Additionally, RNH1-D210N-GFP-expressing cells did not display a replication defects, as illustrated by the number of cells incorporating EdU (Supplementary Figure 3D). Finally, an MTT assay demonstrated that RNH1-WT-GFP and RNH1-D210N-GFP overexpression for 24 h did not alter cell viability (Supplementary Figures 3E and 3F).

To test the association of PARP1 at R-loop sites, we used proximity ligation assay (PLA) coupling a rabbit PARP1 antibody with the mouse RNA–DNA hybrid monoclonal antibody S9.6 in RNH1-WT-GFP and RNH1-D210N-GFP expressing U2OS cells (64). We observed very few PLA foci in untreated or doxycycline-induced RNH1-WT-GFP-expressing cells due to the resolution of the structures. In contrast, we noted an 8-fold increase of PLA foci in RNH1-D210N-GFP-expressing U2OS cells (Figure 3A and B), suggesting that PARP1 is within the proximity of R-loops. To ensure the specificity of the PLA staining, we confirmed that the staining of doxycycline-treated RNH1-D210N-GFP cells with only one of the antibodies did not yield any PLA foci (Supplementary Figure 3G). In addition, we also assessed the formation of PLA foci in U2OS cells transiently transfected with siRNAs against RNH1 or Senataxin (SETX), another RNA–DNA helicase involved in R-loop resolution (38). We verified the knock down of both proteins by western blot (Supplementary Figure 3H) and the subsequent increase of RNA–DNA hybrids by dot blot using the S9.6 antibody (Supplementary Figure 3I). Due to a poor knockdown of RNH1 using siRNA57, we only performed PLA staining on cells transfected with RNH1 siRNA58 and SETX siRNA. Both the knock down of RNH1 and SETX led to a significant increase of PLA foci between the PARP1 and S9.6 antibodies when compared to un-transfected U2OS cells (Figure 3C and D). Our data confirm that an increase in unresolved R-loops correlates with increased PARP1 association with R-loop site formation.

PARP1 association with R-loop-forming site in cells triggers its activity

Simultaneous treatment of cells with DNA damaging agents and PARP1 inhibitors was shown to trigger PARP1 retention at the DNA damage sites and subsequent enrichment of the inactive enzyme on chromatin (65–67). Because our *in vitro* data suggests that R-loops are substrates for PARP1 that also trigger its activity, we hypothesized that their accumulation leads to PARP1 chromatin accumulation upon inhibition of PARP1 activity when RNH1-D210N-GFP is overexpressed. To do this, we first verified that PARP1 activity was triggered upon RNH1-D210N-GFP overexpression by immuno-fluorescence using the 10H anti-PAR antibody. As a positive control, we used the replication inhibitor aphidicolin (APH), which triggers replication stress, fork breakage and subsequent PARP1 activity (Figure 3E and F) (68). The quantification of the nuclear PAR signal mean intensity revealed that PARylation was significantly increased in RNH1-D210N-GFP-expressing cells when compared to un-induced cells (Figure 3E and F). Next, we used the RNH1-WT-GFP and RNH1-D210N-GFP-expressing U2OS cells and isolated the chromatin-bound protein fractions upon treatment with doxycycline and the PARP inhibitor talazoparib ($PARPi^{Tal}$), found to slow down PARP1 release from the DNA (67). Only the RNH1-D210N-GFP-expressing cells displayed a significant enrichment of PARP1 on the chromatin upon inhibition (Figure 3G and H). Accordingly, the number of PLA foci formed between the S9.6 and PARP1 antibodies increased significantly upon doxycycline and $PARPi^{Tal}$ treatment as compared to doxycycline alone (Figure 3I and J). Our single antibody control staining did not yield foci (Supplementary Figure 3J) confirming the specificity of the PLA staining. Taken together, these data

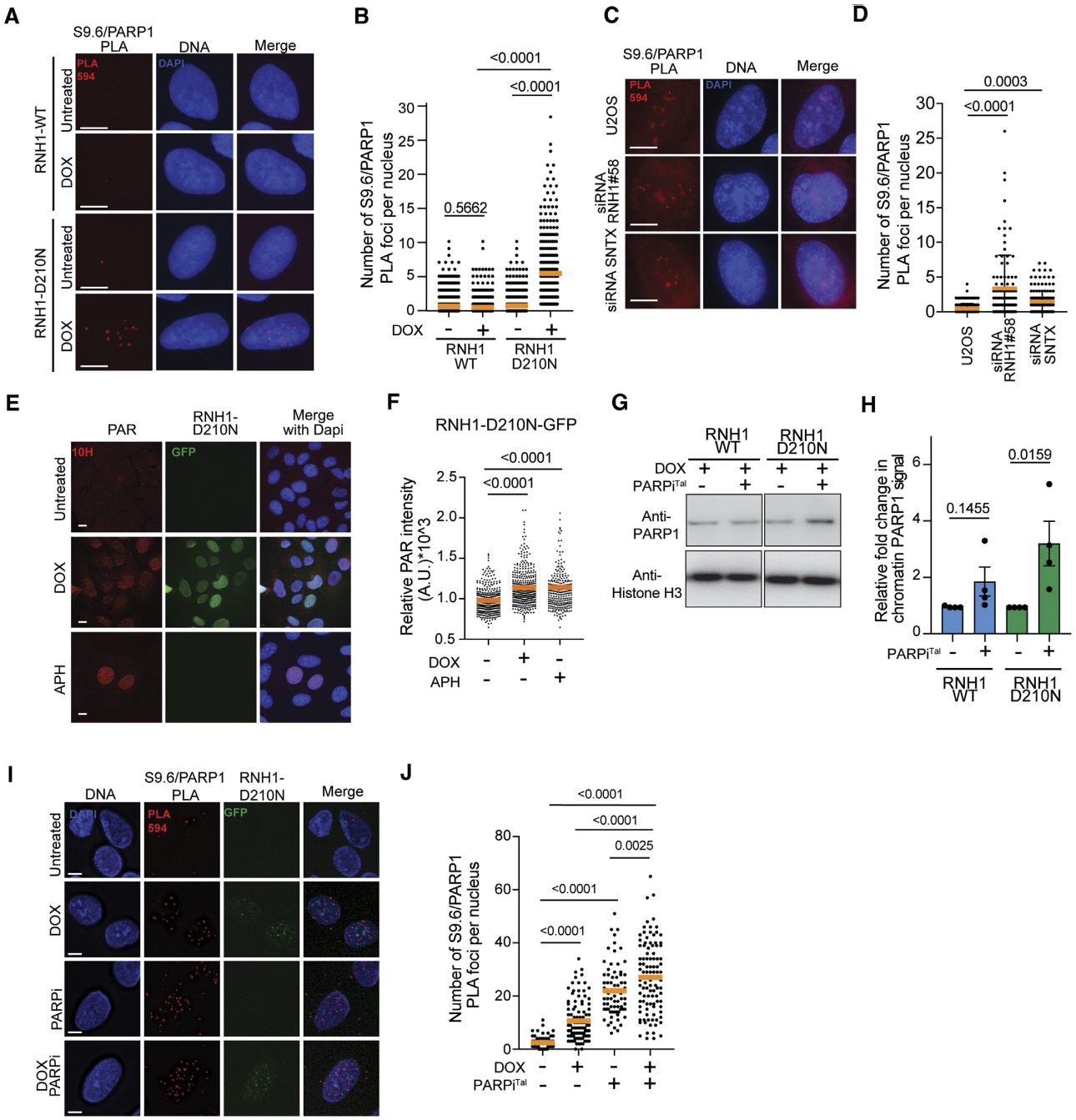

Figure 3. PARP1 associates with R-loop-forming sites in cells. (**A**) Representative images of S9.6:PARP1 PLA in RNH1-WT-GFP and RNH1-D210N-GFP U2OS cells untreated or induced with DOX. PLA foci (red) are observed due to PARP1 antibody association within a 40 nm distance of the S9.6 antibody. White scale bars represent 10 μm. (**B**) Quantification of the number of PLA foci per nucleus for each experimental condition illustrated in (A). Orange bars represent the mean. Data are from three independent experiments with 75 to 100 cells counted per experiment. P values were obtained using ordinary one-way ANOVA. (**C**) Representative images of S9.6:PARP1 PLA analysis in U2OS cells transfected with siRNA for RNH1 or SETX. White scale bars represent 10 μm. (**D**) Quantification of the number of PLA foci per nucleus for each experimental condition illustrated in (C). Orange bars represent the mean. Data are collected from 100 to 170 nuclei. P values were obtained using ordinary one-way ANOVA. (**E**) Representative images of ant-PAR immunofluorescence in RNH1-D210N-GFP U2OS cells. PAR signal is shown in red and RNH1-D210N-GFP expression in green (middle row). DNA is shown in blue after DAPI staining. Aphidicolin (APH) (0.4 μM) was used as a positive control. White scale bars represent 10 μm. (**F**) Quantification of relative PAR signal intensity as shown in (E). Orange bars represent median PAR intensity. Data are from three independent experiments in which 100–150 nuclei were counted for each experiment. *P* values were obtained using one-way ANOVA analysis. (**G**) Western blot analysis of chromatin-bound protein fractions isolated from RNH1-WT-GFP and RNH1-D210N-GFP U2OS cells before and after induction with DOX and treatment with 100 nM talazoparib (PARPi) for 24 hrs. (**H**) Quantification of relative fold change in chromatin PARP1 signal over non-PARPi-treated conditions. Data are from three independent experiments. P values were obtained using Student's *t*-tests. (**I**) Representative images of S9.6:PARP1 PLA analysis in RNH1-D210N-GFP U2OS cells treated with PARPi. RNH1-D210N-GFP expression is shown in green and DNA in blue after DAPI staining. It is to be noted that the dimmer GFP signal is due to the pre-extraction and PLA staining processes (second and bottom row). White scale bars represent 10 μm. (**J**) Quantification of the number of PLA foci per nucleus for each experimental condition illustrated in (I). Orange bars represent the mean. Data are from 100 to 200 nuclei. P values were obtained using ordinary one-way ANOVA.

strongly suggest that PARP1 associates with unresolved R-loop structures in cells.

PARP1 can associate with G4 structures formed at R-loop sites in cells

Although our data in vitro suggest that G4 structures are not necessary for PARP1 binding to R-loops, such interaction between G4s formed within the displaced ssDNA may still occur in cells. Thus, we asked whether PARP1 could also associate with G4s that could potentially form on the displaced ssDNA within R-loop structures in cells. We first used the G4 antibody BG4-FLAG for immunofluorescence in cells overexpressing the RNH1-D210N-GFP mutant. We also treated cells with pyridostatin (PDS), a G4 ligand that stabilizes G4 structures. We observed that addition of doxycycline yielded an increase of BG4 staining intensity that was exacerbated when PDS was added (Supplementary Figure 3K and L). Next, to test the association of PARP1 with G4 structures in cells, we performed a PLA assay using the BG4-FLAG antibody in combination with a PARP1 antibody. The quantification of the nuclear PLA foci revealed an association of PARP1 to G4 structures in cells that was 1.8-fold increased upon R-loop formation (Supplementary Figures 3M and 3N). To ensure the specificity of the PLA staining, we included controls where the PARP1, BG4 or FLAG antibodies were omitted (Supplementary Figure 3O). Our data confirm previous work showing that PARP1 can bind G4 structures in cells (9) and show that this association can occur in the context of R-loop formation.

PARP1 prevents R-loop accumulation

To test a role of PARP1 in the R-loop biology mechanisms, we measured the formation of genomic R-loops in PARP1-depleted U2OS cells (PARP1ko; Figure 4A). First, we extracted the DNA from both PARP1-proficient and -deficient U2OS cells and detected the presence of RNA–DNA hybrids by immuno-slot blot using the S9.6 antibody (Figures 4B and C). Increasing amounts of RNA–DNA hybrids were observed as a function of DNA content for both cell lines while ecRNH treatment eliminated these signals. Importantly, RNA–DNA hybrid levels were significantly higher upon PARP1 knock out (Figures 4B and C).

Next, we detected RNA–DNA hybrids in cells by immunofluorescence. Because the S9.6 antibody can recognize double-stranded RNA (dsRNA) (69) and to ensure the specificity of the signal, the fixed cells were treated with RNase III and RNase T1 which degrade dsRNAs and ssRNAs, respectively, or ecRNH which specifically degrades RNA–DNA hybrids. We first observed an increase in the S9.6 signal intensity in PARP1ko cells (Figures 4D and E). Although the overall S9.6 signal was decreased by a treatment of the cells with RNase III and RNase T1, it remained significantly higher in cells lacking PARP1 (Figures 4D and E). However, the S9.6 signal reached below-background levels following a treatment with the ecRNH in both cell lines (Figures 4D and E), indicating the specificity of the signal. To verify to direct implication of PARP1 in this overall R-loop increase, we complemented PARP1ko cells with a Cas9-insensitive Flag-tagged PARP1 construct (Figure 4F) and performed an S9.6 immuno-dot blot. Our data indicate that PARP1 expression in PARP1ko cells restored the RNA–DNA hybrid amount to a level consistent with the one measured in U2OS cells (Figure 4G). In addition, we also observed an increase of R-loop levels by immunofluorescence in PARP1ko HeLa cells (Supplementary Figure S4A–C), demonstrating that the impact of PARP1 depletion is not cell line-specific.

To look more closely into PARP1-dependent regulation of R-loop levels, we performed RNA–DNA immunoprecipitation (DRIP) in U2OS cells and used qPCR to verify the presence of specific loci that have been identified as prone to R-loop formation, therefore making them suitable for R-loop accumulation analyses. We noted an enrichment of R-loops in PARP1ko cells at the three R-loop-rich regions tested within the beta-actin locus *ACTB* (Figures 4H) and in *EGR1*, *FOS* and *RPL13A* genes (Figure 4I–K). Importantly, when the samples were treated with ecRNH, the levels of R-loops dramatically decreased, confirming that the signal detected was specific for RNA–DNA hybrids (Figure 4H–K). As a negative control, we performed DRIP-qPCR using a probe that binds in a non-R-loop-rich region of the *EGR1* gene, which did not yield any R-loop enrichment in both cell lines (Supplementary Figure 4D). Moreover, R-loop enrichment in PARP1ko cells could not be attributed to an increase in the overall level of transcription in these cells because we did not observe any increase in mRNA levels for each target (Supplementary Figure 4E). Finally, to verify that the increases in R-loop levels were not an artifact of the stable knock out of PARP1, we performed DRIP-qPCR with the same sets of probes in cells transfected with an siRNA against PARP1 (Supplementary Figure 4F), 48 h after transfection. In these conditions, although transcription at the *FOS* gene locus was slightly increased, we did not note an increase in transcription in all the other regions tested (Supplementary Figure 4G). In line with our observations in PARP1ko cells, PARP1 depletion by siRNA triggered an increase in R-loop levels (Supplementary Figures 5H-K). However, this increase did not reach significance for the probes binding to the Poly(A) and Termination sites of the *ACTB* gene, most likely due to the background level of PARP1 remaining in the cells. Taken together, these data demonstrate that the lack of PARP1 leads to an accumulation of RNA–DNA hybrids specifically and suggest a role for PARP1 in the prevention of their formation or their resolution.

PARP1 depletion or inhibition triggers R-loop-mediated genomic instability

During DNA damage induction, PARP1 activity is necessary to recruit DNA repair protein factors to mediate DNA damage resolution, thereby preventing genome instability. Because our data show that PARP1 binds to R-loops which leads to its activation, we asked whether the lack of PARP1 or its activity would be responsible for genomic instability.

First, we tested the effect of PARP inhibition on R-loop levels, by treating the RNH1-D210N-GFP-expressing U2OS cells with PARPi^{Tal} for 24 h followed by immunodetection of R-loops by fluorescence microscopy. Fixed

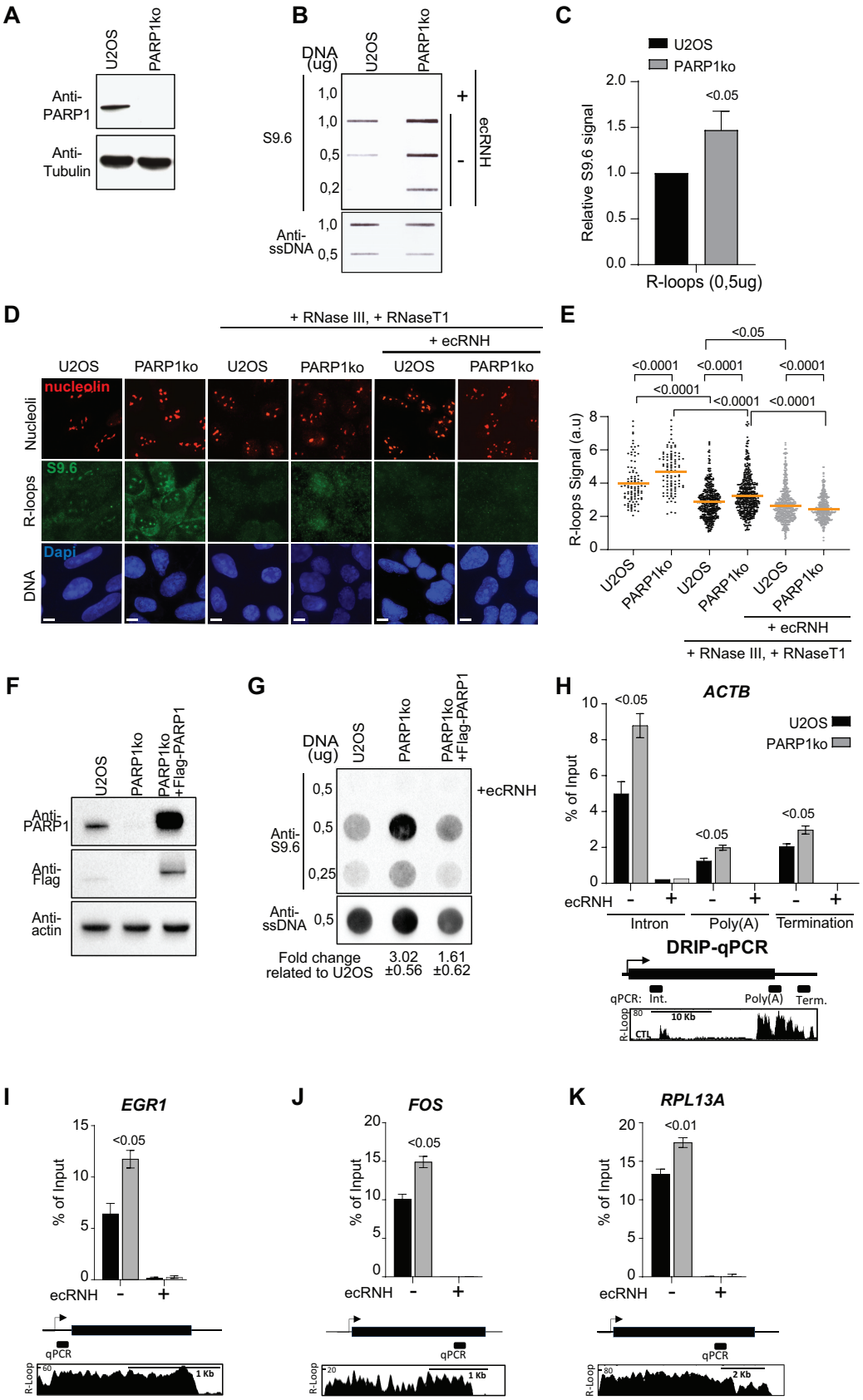

Figure 4. PARP1 prevents R-loop accumulation. (**A**) Anti-PARP1 western blot analysis in U2OS and PARP1ko U2OS cells demonstrating efficient deletion of PARP1. (**B**) Anti-S9.6 immuno-slot blot of genomic DNA extracted from U2OS or PARP1ko cells. ecRNH was used as a negative control to

cells were treated by RNases T1 and III prior to their incubation with the S9.6 antibody to ensure antibody S9.6 binding specificity (Figure 5A). As expected, Doxycycline-induced RNH1-D210N-GFP expression increased R-loop signal intensity. Notably, PARPi^{Tal} treatment also increased R-loops in untreated and doxycycline-treated cells (Figure 5A and B). Moreover, treating fixed cells with ecRNH1 abolished S9.6 signal, confirming that the increased S9.6 intensity in PARPi^{Tal}-treated cells arose from R-loops (Figure 5B). To test whether this impact of PARP1 inhibition could be reproduced in another cell line, we used the HeLa cells expressing RNH1-WT-GFP or RNH1-D210N-GFP upon doxycycline treatment (Supplementary Figure 5A and B). R-loop accumulation was also observed in these cells when treated with the PARP1 inhibitor Olaparib (PARPi^{Ola}) (Supplementary Figure 5C and 5D). However, this increase was prevented by the overexpression of RNH1-WT-GFP (Supplementary Figure 5C and D). Finally, consistent with what we reported with U2OS cells, treatment of RNH1-D210N-GFP-expressing cells with PARPi^{Ola} further increased R-loop levels (Supplementary Figure 5E and F). Our data indicate that PARP1 inhibition prevents R-loop resolution independently of the cell line tested.

To next assess the impact of PARP1 inhibition on genome stability, we followed the gamma H2AX foci (γH2AX) formation by immunofluorescence, an indicator of DNA damage. Although R-loop-associated DDR mechanisms remain elusive, several studies have attributed it to transcription-replication conflicts (18,70–72). Thus, we also pulsed the cells with the nucleotide analogue EdU, 15 min prior to fixation to identify the cells undergoing replication. Because of the various roles played by PARP1 in cells, treatment with PARPi^{Tal} led to a rise in γH2AX foci regardless of the cell replication status (Figure 5C and D). Doxycycline-dependent expression of RNH1-D210N-GFP, however, led to a significant rise in DNA damage only in replicating cells (Figure 5D, pink box). Interestingly, combining PARPi^{Tal} and doxycycline, triggered an increase in the number of γH2AX foci in both non-replicating and replicating cells. Genomic instability in these cells was also accompanied by an augmentation of the average number of micronuclei (Supplementary data 5I). We also noted an increase of γH2AX foci in HeLa cells when expressing the RNH1-D210N-GFP and/or when treated with PARPi^{Ola} (Supplementary Figure 5G and H). Our data indicate that PARP1's role in the prevention of R-loop-associated genome instability is not solely limited to the conflicts between the R-loop and the replication machinery.

To further confirm a direct role for PARP1 in preventing R-loop associated genomic instability we knocked out PARP1 in the RNH1-D210N-GFP expressing U2OS cells. After the isolation of a stable clone, we transfected the cells with our plasmid allowing the expression of the Cas9 insensitive Flag-tagged PARP1 construct (Figure 4F). Consistent with our data obtained upon PARP1 inhibition, PARP1 depletion led to a significant rise of γH2AX foci in DOX-treated cells (Figure 5E and F). We observed a similar increase of γH2AX foci in RNH1-D210N-GFP expressing cells upon transient depletion of PARP1 with siRNA (Supplementary Figure 5J–L). Importantly, the expression of Flag-PARP1 in PARP1ko cells significantly reduced the number of γH2AX foci (Figure 5E and F). Taken together, these data confirm that PARP1 and its activity can play a role in preventing R-loop associated genomic instability.

DISCUSSION

In this study, we demonstrate that the DNA-dependent ART enzyme PARP1 associates with R-loop structures *in vitro* and at R-loop formation sites in cells. Moreover, we show that both genetic deletion and inhibition of PARP1 are responsible for an accumulation of RNA–DNA hybrids in both U2OS and HeLa cells and the subsequent genomic instability that is enhanced when R-loops accumulate. Our data reveal a crucial role for PARP1 in R-loop homeostasis and expand the number of DNA substrates that PARP1 can recognize.

Our study brings two major questions on the PARP1 binding mechanisms on R-loops: where on this complex structure does PARP1 bind and which PARP1 domains are

degrade R-loop structures. The anti-ssDNA antibody was used as a loading control. White scale bars represent 10 μm. (**C**) Quantification of relative S9.6 signal on immuno-slot blot in (B) measured from 0.5 μg DNA. Data are from 3 independent experiments. P value was obtained using a Student's *t*-test. (**D**) S9.6 immunofluorescence in U2OS and PARP1ko cells. S9.6 signal is shown in green and a nucleolin control is shown in red. RNases T1 and III were used to degrade ss- and dsRNAs and increase specificity of S9.6 signal. RNH1 treatment was used as a negative control to degrade R-loop structures. White scale bars represent 10 μm. (**E**) Quantification of relative S9.6 signal observed in (D). Orange bars represent mean S9.6 intensity. Data are from 3 independent experiments. P values were obtained using ordinary one-way ANOVA. (**F**) Western blot analysis of RNH1-D210N-GFP U2OS cells either with PARP1ko and/or PARP1 re-expression by transfection with the 3×-FLAG-PARP1 plasmid. The PARP1 antibody was used to show efficient knockout of PARP1 followed by efficient re-expression upon complementation. The FLAG antibody was used to confirm the presence of FLAG-tagged PARP1 after complementation. (**G**) Anti-S9.6 immuno-dot blot of genomic DNA extracted from U2OS, PARP1ko or PARP1ko cells complemented with Cas9-insensitive Flag-tagged PARP1. ecRNH was used as a negative control to degrade R-loop structures. The anti-ssDNA antibody was used as a loading control. (**H**) (Bottom panel) schematic showing three regions of theβ-actin (ACTB) locus that are prone to R-loop formation. (Top panel) qPCR output of R-loop levels in the three ACTB loci regions chosen in U2OS and PARP1ko cells, demonstrating an increase in R-loop levels upon PARP1ko in all three regions. RNH1 was used as a negative control to degrade R-loop structures. Data are from eight independent experiments. Statistical analysis was performed using a Student's *t*-test. (**I**) (Bottom panel) schematic showing region of the *EGR1* locus that is prone to R-loop formation. (Top panel) qPCR output of R-loop levels in the *EGR1* locus in U2OS and PARP1ko cells, demonstrating an increase in R-loop levels upon PARP1ko. RNH1 was used as a negative control to degrade R-loop structures. Data are from 8 independent experiments. P value was obtained using a Student's *t*-test. (**J**) (Bottom panel) schematic showing region of the *FOS* locus that is prone to R-loop formation. (Top panel) qPCR output of R-loop levels in the *FOS* locus in U2OS and PARP1ko cells, demonstrating an increase in R-loop levels upon PARP1ko. RNH1 was used as a negative control to degrade R-loop structures. Data are from 8 independent experiments. *P* value was obtained using a Student's *t*-test. (**K**) (Bottom panel) schematic showing region of the *RPL13A* locus that is prone to R-loop formation. (Top panel) qPCR output of R-loop levels in the *RPL13A* locus in U2OS and PARP1ko cells, demonstrating an increase in R-loop levels upon PARP1ko. RNH1 was used as a negative control to degrade R-loop structures. Data are from 8 independent experiments. P value was obtained using a Student's *t*-test.

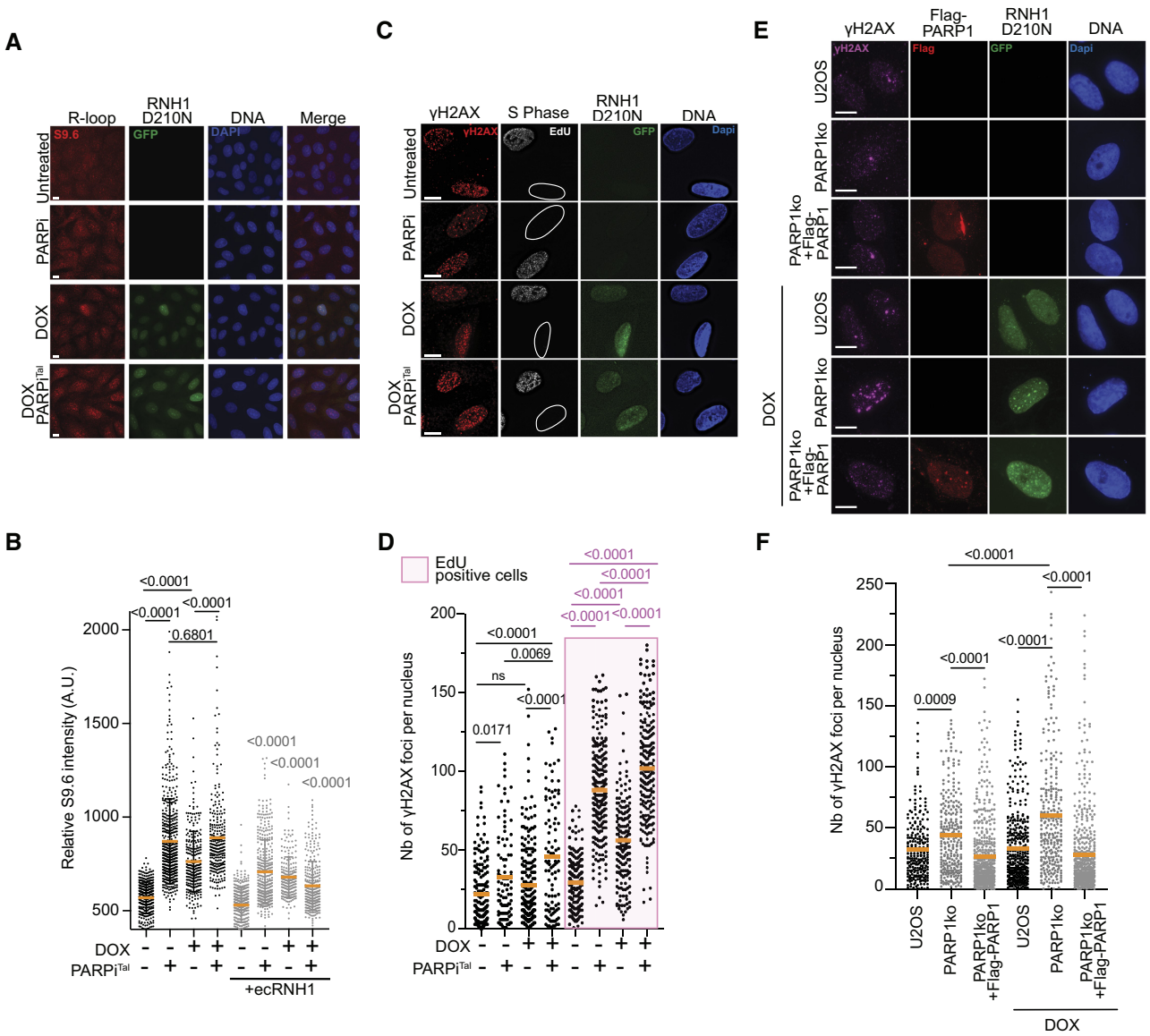

Figure 5. PARP1 depletion or inhibition triggers R-loop-mediated genomic instability. (**A**) Representative images of anti-S9.6 immuno-fluorescence in RNH1-D210N-GFP-expressing U2OS cells treated with DOX and/or PARPi^{Tal}. RNases T1 and III were used to degrade unspecific RNAs. S9.6 signal is shown in red, RNH1-D210N-GFP in green, and DNA in blue after DAPI staining. White scale bars represent 10 μm. (**B**) Quantification of relative S9.6 signal intensity from S9.6 immuno-fluorescence shown in (A). Data in black are from cells treated with RNases T1 and III and data in grey are from cells treated with RNases T1, III and H1. Orange bars represent mean S9.6 intensity. Data were collected from three independent experiments in which 100–200 nuclei per condition were counted. Statistical analyses were performed using ordinary one-way ANOVA. (**C**) Representative images of anti-γH2AX immunofluorescence in RNH1-D210N-GFP-expressing U2OS cells treated with DOX and/or PARPi for 24 h and pulsed with EdU for 15 min prior to fixation. γH2AX foci are shown in red, DNA is shown in blue after DAPI staining, and EdU signal is shown in grey. EdU-negative nuclei are outlined in white. White scale bars represent 10 μm. (**D**) Quantification of the number of γH2AX foci per nucleus for each experimental condition shown in (C). The pink box represents EdU-positive nuclei. Orange bars represent the mean. Data are from three individual experiments in which 80–150 nuclei were counted per condition. Statistical analyses were performed using ordinary one-way ANOVA. (**E**) Representative images of anti-γH2AX immunofluorescence in RNH1-D210N-GFP-expressing U2OS cells, RNH1-D210N-GFP-expressing PARP1ko U2OS cells and RNH1-D210N-GFP-expressing PARP1ko U2OS cells complemented with Cas9-insensitive Flag-PARP1. γH2AX foci are shown in red, DNA is shown in blue after DAPI staining. White scale bars represent 10 μm. (**F**) Quantification of the number of γH2AX foci per nucleus for each experimental condition shown in (E). Data were collected from three independent experiments in which 300–500 nuclei per condition were counted. Statistical analyses were performed using ordinary one-way ANOVA.

involved? PARP1 is well known to bind SSBs and DSBs as well as a variety of non-B DNA structures such as cruciforms, hairpins, DNA overhangs, stalled replication forks and G4s (6,7,9,73–75). PARP1 also binds to undamaged DNA, however, unlike broken DNA or non-B DNA structures, this does not trigger its activity (76–78). In agreement with this, we show that PARP1 can bind plasmid molecules but auto-PARylation is only triggered when they harbor R-loop structures. Moreover, it also suggests that PARP1 binding to R-loop structures enables the conformational change that is necessary to promote its catalytic activation. This conformational change was shown to involve the zinc fingers 1 and 3 (ZN1 and ZN3) as well as the WGR domain. Binding to DNA breaks via these domains results in the unfolding of the helical subdomain which facilitates access of NAD^+ to the active site (54,79,80). However, the binding mechanisms of PARP1 to non-B DNA structures are less documented. So far, one study suggested that PARP1 binding to G4s may involve its ZN1 domain (6). Although, R-loops harbor a displaced non-template single-stranded DNA that can form G4s (57,58), our data demonstrated that G4s are not necessary for PARP1 association with R-loops and for its activation. However, our EMSA assays revealed that the displaced ssDNA may be an important factor in PARP1 binding. One limitation of our assay resides in the presence of similar dsDNA ends in the dsDNA, Loop, D-loop and R-loop substrates for which PARP1 has a strong affinity. Nonetheless, statistical analyses demonstrated that PARP1 binds with a greater affinity to an R-loop than to a paired RNA–DNA hybrid or RNA alone. Furthermore, PARP1 showed more affinity to an R-loop than a D-loop while showing higher affinity to ssDNA and loop substrates. Altogether, this suggests that PARP1 that the displaced ssDNA of the R-loop contributes to the recognition of the structure by PARP1. Moreover, R-loops can adopt a wild range of sizes and their stability varies depending on the site or context of formation (promoters, gene bodies or DSBs) (18) which can potentially impact and modulate the binding of PARP1. Verifying the nature specific or unspecific of the type of R-loop enriched in PARP1ko cells, would require a whole genome R-loop mapping. Clearly, more studies are needed to fully understand the binding mechanisms of PARP1 to the R-loop structures.

One of the primary roles of PARP1 when binding to DNA breaks and associating with a stalled replication fork or even a G4 is to facilitate the PAR-dependent recruitment of downstream proteins involved in the repair and resolution of these breaks and structures (8,74,81). Here, we report that PARP1 inhibition or depletion using CRISPR or siRNA trigger R-loop accumulation and is responsible for an increase in R-loop associated genomic instability. Because our data show that PARP1 binds R-loops, our work suggests that PARP1 may be involved in one of the mechanisms that can mediate the resolution of these structures in cells. In line with our data, a recent study has also reported an increase of R-loop levels in PARP1-depleted cells (39). Interestingly, several ATP-dependent RNA helicases harboring an RNA–DNA unwinding activity such as the Bloom syndrome helicase (BLM), the DEAD-box helicases DDX1, DDX5, DDX39 (UAP56) or the DExH-Box helicase DHX9 (45,82–84) have been identified in various independent mass spectrometry analyses of PAR interacting proteins (85–88). This could suggest that the non-covalent PAR-binding and/or ADP-ribosylation of these helicases to PAR may impact their recruitment at R-loop sites and/or their unwinding activities. In support with this hypothesis, PARP1 activity was shown to promote the recruitment of the RNA helicase DDX18 at R-loop formation sites via DDX18 interaction with the PAR polymers. Interestingly, this DDX18 interaction with PARylated PARP1 was associated to both the prevention of R-loop associated replication defects and R-loop-mediated DNA break resolution (39).

The increase in γH2AX foci formation upon RNH1-D210N-GFP-dependent R-loop accumulation that we report here, confirms previous observations showing that R-loops are sources of DNA damage and overall genome instability (89–91). R-loops can impact genomic stability in several ways. For instance, the single-stranded DNA formed by the displaced non-template DNA is highly susceptible to the activity of nucleases including FEN1 or XPG and XPF (83,92) which eventually leads to the formation of DSBs. Additionally, the ssDNA can be targeted by activation-induced deaminase (AID) that converts cytosines into uracil which are in turn removed by the BER glycosylase UNG (93), inducing SSBs that are substrates for PARP1. The displaced ssDNA was also shown to be coated by the ssDNA proteins RPA necessary for recruitment of RNase H1 at R-loop sites (42). It is noteworthy that PAR was found to favor the recruitment of RPA proteins in cells and *in vitro* (94). R-loops can also cause collisions between the transcription and the replication machinery and the stalling of a replication fork at an unresolved R-loop can trigger replication stress and the formation of DSBs. PARP1 and PAR metabolism have been extensively described as crucial factors in the replication stress management and replication fork restart mechanisms (74,94–96). Thus, while our data clearly demonstrate that R-loops are PARP1 targets, the recruitment of PARP1 and subsequent PARylation activity observed in U2OS cells, could be also attributed to these various mechanisms through which R-loops impact the genome.

Besides an apparent involvement of R-loops in genomic instability, many studies report that DNA breaks can lead to the formation of R-loops to promote the repair of the break. For instance, the treatment of cells with camptothechin (CPT) induces the persistence of topoisomerase I-DNA cleavage complexes, leading to an increase in DNA breaks and also of R-loop levels (97). Interestingly, PARP1 has been associated with R-loop-mediated DSB formation upon CPT treatment (83,98). A consequence of CPT-dependent R-loop accumulation is the PARylation and recruitment of TonEBP for the mediation of R-loop resolution (98). A direct interaction between DExH-Box helicase DHX9 and PARP1 was also described in this context, yet the recruitment of the helicase was independent of this interaction (83). More recently, a study reported that ATM-deficient cells accumulate transcription-dependent R-loops and single-stranded DNA breaks upon oxidative stress, leading to an activation of PARP1 and PARP2 that is abrogated following overexpression of the RNA–DNA helicase SETX (40). Very interestingly, in this work, the authors observed that PAR promotes protein aggregation. PAR-

seeded liquid-demixing of intrinsically disordered proteins has been shown to be the biological process underlying protein aggregation (99). Several proteins involved in R-loop processing promote the assembly of liquid-liquid phase separation (LLPS)-mediated membrane-less R-loop foci (100). Similarly, our AFM data revealed that activated PARP1 could form complexes with multiple R-loop molecules bridged by the protein. These data were collected by incubation for 10 min on ice because the regular 5-min room temperature incubation led to the formation of aggregates. It is therefore possible that the protein aggregates found in ATM-deficient cells are formed via PARP1 binding to the R-loop structures found abundantly in these cells (40).

In conclusion, our study uncovers R-loops as novel physiological substrates that drive PARP1 activation. We highlight that PARP1 binds to R-loops and that its activation can potentially mediate their resolution. Our work also suggests a role for PARP1 in the management of R-loop-associated genomic instability. R-loops are crucial for various cellular processes but harmful if unscheduled or unresolved. Unbalanced R-loop homeostasis can be at the origin of several human diseases including cancers and neurodegenerative diseases (90,91). Understanding how PARP1 can prevent, mediate, or resolve these structures will prove crucial in the therapeutic management of these human diseases. PARPi are currently used for the treatment of many cancers including breast, ovarian, and prostate cancers and are being tested in more than 500 clinical trials. Thus, our findings have direct implications for the clinical use and effectiveness of PARP inhibition in the clinical treatment of various malignancies.

SUPPLEMENTARY DATA

Supplementary Data are available at NAR Online.

ACKNOWLEDGEMENTS

We thank Peggy Hempstead (E.F. lab) and Yan Coulombe (J.Y.M. lab) for technical support and Dr. Anna Pluciennik (Thomas Jefferson University) for feedback and helpful discussions. We thank Dr. Shikhar Uttam (University of Pittsburgh) for help with statistical analyses. We thank Dr. Sara Selig (Israel Institute of Technology, Haifa) for providing the pFC-mAIRN plasmid.

FUNDING

National Institute of Health [R00ES027028]; UPMC Hillman Cancer Center and the Sydney Kimmel Cancer center at Thomas Jefferson University (to E.F.); FDN-388879 (to J.Y.M.); CIHR MOP-418863 (to G.P.); CIHR PJT-173370 (to J.M.P.); P. Edward Evans Foundation; American Society of Hematology Scholar Award the 2022 AACR Career Development Award to Further Diversity, Equity, and Inclusion in Cancer Research, which is supported by Merck [22-20-68-NGUY]; National Institutes of Health's National Center for Advancing Translational Sciences [KL2TR002492 and UL1TR002494]; NHLBI [R01HL163011 to H.D.N.]; Thomas Jefferson University and Sidney Kimmel Cancer center (to E.F.); Masonic Cancer Center, University of Minnesota (to H.D.N); J.Y.M. is a Tier I Canada Research Chair in DNA repair and Cancer Therapeutics; S.Y.M. is a FRQS postdoctoral fellow; E.F. is an Innovative Cancer Research Program Hillman fellow. Funding for open access charge: NIH.
Conflict of interest statement. None declared.

REFERENCES

1. Matta,E., Kiribayeva,A., Khassenov,B., Matkarimov,B.T. and Ishchenko,A.A. (2020) Insight into DNA substrate specificity of PARP1-catalysed DNA poly(ADP-ribosyl)ation. *Sci. Rep.*, **10**, 3699.
2. Luscher,B., Ahel,I., Altmeyer,M., Ashworth,A., Bai,P., Chang,P., Cohen,M., Corda,D., Dantzer,F., Daugherty,M.D. *et al.* (2021) ADP-ribosyltransferases, an update on function and nomenclature. *FEBS J.*, **289**, 7399–7410.
3. Groslambert,J., Prokhorova,E. and Ahel,I. (2021) ADP-ribosylation of DNA and RNA. *DNA Repair (Amst.)*, **105**, 103144.
4. Langelier,M.F., Riccio,A.A. and Pascal,J.M. (2014) PARP-2 and PARP-3 are selectively activated by 5' phosphorylated DNA breaks through an allosteric regulatory mechanism shared with PARP-1. *Nucleic Acids Res.*, **42**, 7762–7775.
5. Lonskaya,I., Potaman,V.N., Shlyakhtenko,L.S., Oussatcheva,E.A., Lyubchenko,Y.L. and Soldatenkov,V.A. (2005) Regulation of poly(ADP-ribose) polymerase-1 by DNA structure-specific binding. *J. Biol. Chem.*, **280**, 17076–17083.
6. Fekete,A., Kenesi,E., Hunyadi-Gulyas,E., Durgo,H., Berko,B., Dunai,Z.A. and Bauer,P.I. (2012) The guanine-quadruplex structure in the human c-myc gene's promoter is converted into B-DNA form by the human poly(ADP-ribose)polymerase-1. *PLoS One*, **7**, e42690.
7. Salvati,E., Botta,L., Amato,J., Di Leva,F.S., Zizza,P., Gioiello,A., Pagano,B., Graziani,G., Tarsounas,M., Randazzo,A. *et al.* (2017) Lead discovery of dual G-quadruplex stabilizers and poly(ADP-ribose) polymerases (PARPs) inhibitors: a new avenue in anticancer treatment. *J. Med. Chem.*, **60**, 3626–3635.
8. Salvati,E., Scarsella,M., Porru,M., Rizzo,A., Iachettini,S., Tentori,L., Graziani,G., D'Incalci,M., Stevens,M.F., Orlandi,A. *et al.* (2010) PARP1 is activated at telomeres upon G4 stabilization: possible target for telomere-based therapy. *Oncogene*, **29**, 6280–6293.
9. Soldatenkov,V.A., Vetcher,A.A., Duka,T. and Ladame,S. (2008) First evidence of a functional interaction between DNA quadruplexes and poly(ADP-ribose) polymerase-1. *ACS Chem. Biol.*, **3**, 214–219.
10. Kim,D.S., Camacho,C.V., Nagari,A., Malladi,V.S., Challa,S. and Kraus,W.L. (2019) Activation of PARP-1 by snoRNAs controls ribosome biogenesis and cell growth via the RNA helicase DDX21. *Mol. Cell*, **75**, 1270–1285.
11. Nakamoto,M.Y., Rudolph,J., Wuttke,D.S. and Luger,K. (2019) Nonspecific binding of RNA to PARP1 and PARP2 does not lead to catalytic activation. *Biochemistry*, **58**, 5107–5111.
12. Cristini,A., Groh,M., Kristiansen,M.S. and Gromak,N. (2018) RNA/DNA hybrid interactome identifies DXH9 as a molecular player in transcriptional termination and R-loop-associated DNA damage. *Cell Rep.*, **23**, 1891–1905.
13. Mosler,T., Conte,F., Longo,G.M.C., Mikicic,I., Kreim,N., Mockel,M.M., Petrosino,G., Flach,J., Barau,J., Luke,B. *et al.* (2021) R-loop proximity proteomics identifies a role of DDX41 in transcription-associated genomic instability. *Nat. Commun.*, **12**, 7314.
14. Roy,D., Yu,K. and Lieber,M.R. (2008) Mechanism of R-loop formation at immunoglobulin class switch sequences. *Mol. Cell. Biol.*, **28**, 50–60.
15. Belotserkovskii,B.P., Tornaletti,S., D'Souza,A.D. and Hanawalt,P.C. (2018) R-loop generation during transcription: formation, processing and cellular outcomes. *DNA Repair (Amst.)*, **71**, 69–81.
16. Aguilera,A. and Garcia-Muse,T. (2012) R loops: from transcription byproducts to threats to genome stability. *Mol. Cell*, **46**, 115–124.
17. Hamperl,S. and Cimprich,K.A. (2014) The contribution of co-transcriptional RNA:DNA hybrid structures to DNA damage and genome instability. *DNA Repair (Amst.)*, **19**, 84–94.
18. Castillo-Guzman,D. and Chedin,F. (2021) Defining R-loop classes and their contributions to genome instability. *DNA Repair (Amst.)*, **106**, 103182.

19. Santos-Pereira,J.M. and Aguilera,A. (2015) R loops: new modulators of genome dynamics and function. *Nat. Rev. Genet.*, **16**, 583–597.
20. Ginno,P.A., Lott,P.L., Christensen,H.C., Korf,I. and Chedin,F. (2012) R-loop formation is a distinctive characteristic of unmethylated human CpG island promoters. *Mol. Cell*, **45**, 814–825.
21. Ginno,P.A., Lim,Y.W., Lott,P.L., Korf,I. and Chedin,F. (2013) GC skew at the 5' and 3' ends of human genes links R-loop formation to epigenetic regulation and transcription termination. *Genome Res.*, **23**, 1590–1600.
22. Toubiana,S. and Selig,S. (2018) DNA:RNA hybrids at telomeres - when it is better to be out of the (R) loop. *FEBS J.*, **285**, 2552–2566.
23. Wahba,L. and Koshland,D. (2013) The Rs of biology: r-loops and the regulation of regulators. *Mol. Cell*, **50**, 611–612.
24. Aronica,L., Kasparek,T., Ruchman,D., Marquez,Y., Cipak,L., Cipakova,I., Anrather,D., Mikolaskova,B., Radtke,M., Sarkar,S. *et al.* (2016) The spliceosome-associated protein Nrl1 suppresses homologous recombination-dependent R-loop formation in fission yeast. *Nucleic Acids Res.*, **44**, 1703–1717.
25. Feretzaki,M., Pospisilova,M., Valador Fernandes,R., Lunardi,T., Krejci,L. and Lingner,J. (2020) RAD51-dependent recruitment of TERRA lncRNA to telomeres through R-loops. *Nature*, **587**, 303–308.
26. Ngo,G.H.P., Grimstead,J.W. and Baird,D.M. (2021) UPF1 promotes the formation of R loops to stimulate DNA double-strand break repair. *Nat. Commun.*, **12**, 3849.
27. Yu,K., Chedin,F., Hsieh,C.L., Wilson,T.E. and Lieber,M.R. (2003) R-loops at immunoglobulin class switch regions in the chromosomes of stimulated B cells. *Nat. Immunol.*, **4**, 442–451.
28. Nakama,M., Kawakami,K., Kajitani,T., Urano,T. and Murakami,Y. (2012) DNA-RNA hybrid formation mediates RNAi-directed heterochromatin formation. *Genes Cells*, **17**, 218–233.
29. Kabeche,L., Nguyen,H.D., Buisson,R. and Zou,L. (2018) A mitosis-specific and R loop-driven ATR pathway promotes faithful chromosome segregation. *Science*, **359**, 108–114.
30. Giordano,A.M.S., Luciani,M., Gatto,F., Abou Alezz,M., Beghe,C., Della Volpe,L., Migliara,A., Valsoni,S., Genua,M., Dzieciatkowska,M. *et al.* (2022) DNA damage contributes to neurotoxic inflammation in Aicardi-Goutieres syndrome astrocytes. *J. Exp. Med.*, **219**, e20211121.
31. Chatzidoukaki,O., Stratigi,K., Goulielmaki,E., Niotis,G., Akalestou-Clocher,A., Gkirtzimanaki,K., Zafeiropoulos,A., Altmuller,J., Topalis,P. and Garinis,G.A. (2021) R-loops trigger the release of cytoplasmic ssDNAs leading to chronic inflammation upon DNA damage. *Sci. Adv.*, **7**, eabj5769.
32. Sagie,S., Toubiana,S., Hartono,S.R., Katzir,H., Tzur-Gilat,A., Havazelet,S., Francastel,C., Velasco,G., Chedin,F. and Selig,S. (2017) Telomeres in ICF syndrome cells are vulnerable to DNA damage due to elevated DNA:RNA hybrids. *Nat. Commun.*, **8**, 14015.
33. Graf,M., Bonetti,D., Lockhart,A., Serhal,K., Kellner,V., Maicher,A., Jolivet,P., Teixeira,M.T. and Luke,B. (2017) Telomere length determines TERRA and R-loop regulation through the cell cycle. *Cell*, **170**, 72–85.
34. Pfeiffer,V., Crittin,J., Grolimund,L. and Lingner,J. (2013) The THO complex component Thp2 counteracts telomeric R-loops and telomere shortening. *EMBO J.*, **32**, 2861–2871.
35. Petti,E., Buemi,V., Zappone,A., Schillaci,O., Broccia,P.V., Dinami,R., Matteoni,S., Benetti,R. and Schoeftner,S. (2019) SFPQ and NONO suppress RNA:dNA-hybrid-related telomere instability. *Nat. Commun.*, **10**, 1001.
36. San Martin-Alonso,M., Soler-Oliva,M.E., Garcia-Rubio,M., Garcia-Muse,T. and Aguilera,A. (2021) Harmful R-loops are prevented via different cell cycle-specific mechanisms. *Nat. Commun.*, **12**, 4451.
37. San Martin Alonso,M. and Noordermeer,S.M. (2021) Untangling the crosstalk between BRCA1 and R-loops during DNA repair. *Nucleic Acids Res.*, **49**, 4848–4863.
38. Skourti-Stathaki,K., Proudfoot,N.J. and Gromak,N. (2011) Human senataxin resolves RNA/DNA hybrids formed at transcriptional pause sites to promote Xrn2-dependent termination. *Mol. Cell*, **42**, 794–805.
39. Lin,W.L., Chen,J.K., Wen,X., He,W., Zarceno,G.A., Chen,Y., Chen,S., Paull,T.T. and Liu,H.W. (2022) DDX18 prevents R-loop-induced DNA damage and genome instability via PARP-1. *Cell Rep.*, **40**, 111089.
40. Lee,J.H., Ryu,S.W., Ender,N.A. and Paull,T.T. (2021) Poly-ADP-ribosylation drives loss of protein homeostasis in ATM and Mre11 deficiency. *Mol. Cell*, **81**, 1515–1533.
41. Patidar,P.L., Viera,T., Morales,J.C., Singh,N., Motea,E.A., Khandelwal,M. and Fattah,F.J. (2020) XRN2 interactome reveals its synthetic lethal relationship with PARP1 inhibition. *Sci. Rep.*, **10**, 14253.
42. Nguyen,H.D., Yadav,T., Giri,S., Saez,B., Graubert,T.A. and Zou,L. (2017) Functions of replication protein A as a sensor of R loops and a regulator of RNaseH1. *Mol. Cell*, **65**, 832–847.
43. Langelier,M.F., Steffen,J.D., Riccio,A.A., McCauley,M. and Pascal,J.M. (2017) Purification of DNA damage-dependent PARPs from *E. coli* for structural and biochemical analysis. *Methods Mol. Biol.*, **1608**, 431–444.
44. Pan,H., Jin,M., Ghadiyaram,A., Kaur,P., Miller,H.E., Ta,H.M., Liu,M., Fan,Y., Mahn,C. and Gorthi,A. (2020) Cohesin SA1 and SA2 are RNA binding proteins that localize to RNA containing regions on DNA. *Nucleic Acids Res.*, **48**, 5639–5655.
45. Mersaoui,S.Y., Yu,Z., Coulombe,Y., Karam,M., Busatto,F.F., Masson,J.Y. and Richard,S. (2019) Arginine methylation of the DDX5 helicase RGG/RG motif by PRMT5 regulates resolution of RNA:DNA hybrids. *EMBO J.*, **38**, e100986.
46. Smolka,J.A., Sanz,L.A., Hartono,S.R. and Chedin,F. (2021) Recognition of RNA by the S9.6 antibody creates pervasive artifacts when imaging RNA:DNA hybrids. *J. Cell Biol.*, **220**, e202004079.
47. Villarreal,O.D., Mersaoui,S.Y., Yu,Z., Masson,J.Y. and Richard,S. (2020) Genome-wide R-loop analysis defines unique roles for DDX5, XRN2, and PRMT5 in DNA/RNA hybrid resolution. *Life Sci. Alliance*, **3**, e202000762.
48. Liu,L., Kong,M., Gassman,N.R., Freudenthal,B.D., Prasad,R., Zhen,S., Watkins,S.C., Wilson,S.H. and Van Houten,B. (2017) PARP1 changes from three-dimensional DNA damage searching to one-dimensional diffusion after auto-PARylation or in the presence of APE1. *Nucleic Acids Res.*, **45**, 12834–12847.
49. Carrasco-Salas,Y., Malapert,A., Sulthana,S., Molcrette,B., Chazot-Franguiadakis,L., Bernard,P., Chedin,F., Faivre-Moskalenko,C. and Vanoosthuyse,V. (2019) The extruded non-template strand determines the architecture of R-loops. *Nucleic Acids Res.*, **47**, 6783–6795.
50. Bou-Nader,C., Bothra,A., Garboczi,D.N., Leppla,S.H. and Zhang,J. (2022) Structural basis of R-loop recognition by the S9.6 monoclonal antibody. *Nat. Commun.*, **13**, 1641.
51. Yang,Y., Wang,H. and Erie,D.A. (2003) Quantitative characterization of biomolecular assemblies and interactions using atomic force microscopy. *Methods*, **29**, 175–187.
52. Pan,H., Jin,M., Ghadiyaram,A., Kaur,P., Miller,H.E., Ta,H.M., Liu,M., Fan,Y., Mahn,C., Gorthi,A. *et al.* (2020) Cohesin SA1 and SA2 are RNA binding proteins that localize to RNA containing regions on DNA. *Nucleic Acids Res.*, **48**, 5639–5655.
53. Lin,J., Countryman,P., Buncher,N., Kaur,P., E,L., Zhang,Y., Gibson,G., You,C., Watkins,S.C., Piehler,J. *et al.* (2014) TRF1 and TRF2 use different mechanisms to find telomeric DNA but share a novel mechanism to search for protein partners at telomeres. *Nucleic Acids Res.*, **42**, 2493–2504.
54. Eustermann,S., Wu,W.F., Langelier,M.F., Yang,J.C., Easton,L.E., Riccio,A.A., Pascal,J.M. and Neuhaus,D. (2015) Structural basis of detection and signaling of DNA single-strand breaks by human PARP-1. *Mol. Cell*, **60**, 742–754.
55. Rudolph,J., Jung,K. and Luger,K. (2022) Inhibitors of PARP: number crunching and structure gazing. *Proc. Natl. Acad. Sci. U.S.A.*, **119**, e2121979119.
56. Roberts,R.W. and Crothers,D.M. (1992) Stability and properties of double and triple helices: dramatic effects of RNA or DNA backbone composition. *Science*, **258**, 1463–1466.
57. De Magis,A., Manzo,S.G., Russo,M., Marinello,J., Morigi,R., Sordet,O. and Capranico,G. (2019) DNA damage and genome instability by G-quadruplex ligands are mediated by R loops in human cancer cells. *Proc. Natl. Acad. Sci. U.S.A.*, **116**, 816–825.
58. Duquette,M.L., Handa,P., Vincent,J.A., Taylor,A.F. and Maizels,N. (2004) Intracellular transcription of G-rich DNAs induces

formation of G-loops, novel structures containing G4 DNA. *Genes Dev.*, **18**, 1618–1629.
59. Cerritelli,S.M., Frolova,E.G., Feng,C., Grinberg,A., Love,P.E. and Crouch,R.J. (2003) Failure to produce mitochondrial DNA results in embryonic lethality in Rnaseh1 null mice. *Mol. Cell*, **11**, 807–815.
60. Al-Behadili,A., Uhler,J.P., Berglund,A.K., Peter,B., Doimo,M., Reyes,A., Wanrooij,S., Zeviani,M. and Falkenberg,M. (2018) A two-nuclease pathway involving RNase H1 is required for primer removal at human mitochondrial OriL. *Nucleic Acids Res.*, **46**, 9471–9483.
61. Murante,R.S., Henricksen,L.A. and Bambara,R.A. (1998) Junction ribonuclease: an activity in Okazaki fragment processing. *Proc. Natl. Acad. Sci. U.S.A.*, **95**, 2244–2249.
62. Rumbaugh,J.A., Murante,R.S., Shi,S. and Bambara,R.A. (1997) Creation and removal of embedded ribonucleotides in chromosomal DNA during mammalian Okazaki fragment processing. *J. Biol. Chem.*, **272**, 22591–22599.
63. Huang,L., Kim,Y., Turchi,J.J. and Bambara,R.A. (1994) Structure-specific cleavage of the RNA primer from Okazaki fragments by calf thymus RNase HI. *J. Biol. Chem.*, **269**, 25922–25927.
64. Boguslawski,S.J., Smith,D.E., Michalak,M.A., Mickelson,K.E., Yehle,C.O., Patterson,W.L. and Carrico,R.J. (1986) Characterization of monoclonal antibody to DNA.RNA and its application to immunodetection of hybrids. *J. Immunol. Methods*, **89**, 123–130.
65. Murai,J., Huang,S.Y., Renaud,A., Zhang,Y., Ji,J., Takeda,S., Morris,J., Teicher,B., Doroshow,J.H. and Pommier,Y. (2014) Stereospecific PARP trapping by BMN 673 and comparison with olaparib and rucaparib. *Mol. Cancer Ther.*, **13**, 433–443.
66. Shen,Y., Aoyagi-Scharber,M. and Wang,B. (2015) Trapping poly(ADP-ribose) polymerase. *J. Pharmacol. Exp. Ther.*, **353**, 446–457.
67. Zandarashvili,L., Langelier,M.F., Velagapudi,U.K., Hancock,M.A., Steffen,J.D., Billur,R., Hannan,Z.M., Wicks,A.J., Krastev,D.B., Pettitt,S.J. *et al.* (2020) Structural basis for allosteric PARP-1 retention on DNA breaks. *Science*, **368**, eaax6367.
68. Hanzlikova,H. and Caldecott,K.W. (2019) Perspectives on PARPs in S Phase. *Trends Genet.*, **35**, 412–422.
69. Hartono,S.R., Malapert,A., Legros,P., Bernard,P., Chedin,F. and Vanoosthuyse,V. (2018) The affinity of the S9.6 antibody for double-stranded RNAs impacts the accurate mapping of R-loops in fission yeast. *J. Mol. Biol.*, **430**, 272–284.
70. Chen,L., Chen,J.Y., Huang,Y.J., Gu,Y., Qiu,J., Qian,H., Shao,C., Zhang,X., Hu,J., Li,H. *et al.* (2018) The augmented R-loop is a unifying mechanism for myelodysplastic syndromes induced by high-risk splicing factor mutations. *Mol. Cell*, **69**, 412–425.
71. Edwards,D.S., Maganti,R., Tanksley,J.P., Luo,J., Park,J.J.H., Balkanska-Sinclair,E., Ling,J. and Floyd,S.R. (2020) BRD4 prevents R-loop formation and transcription-replication conflicts by ensuring efficient transcription elongation. *Cell Rep.*, **32**, 108166.
72. Lam,F.C., Kong,Y.W., Huang,Q., Vu Han,T.L., Maffa,A.D., Kasper,E.M. and Yaffe,M.B. (2020) BRD4 prevents the accumulation of R-loops and protects against transcription-replication collision events and DNA damage. *Nat. Commun.*, **11**, 4083.
73. D'Silva,I., Pelletier,J.D., Lagueux,J., D'Amours,D., Chaudhry,M.A., Weinfeld,M., Lees-Miller,S.P. and Poirier,G.G. (1999) Relative affinities of poly(ADP-ribose) polymerase and DNA-dependent protein kinase for DNA strand interruptions. *Biochim. Biophys. Acta*, **1430**, 119–126.
74. Bryant,H.E., Petermann,E., Schultz,N., Jemth,A.S., Loseva,O., Issaeva,N., Johansson,F., Fernandez,S., McGlynn,P. and Helleday,T. (2009) PARP is activated at stalled forks to mediate Mre11-dependent replication restart and recombination. *EMBO J.*, **28**, 2601–2615.
75. Langelier,M.F., Planck,J.L., Roy,S. and Pascal,J.M. (2011) Crystal structures of poly(ADP-ribose) polymerase-1 (PARP-1) zinc fingers bound to DNA: structural and functional insights into DNA-dependent PARP-1 activity. *J. Biol. Chem.*, **286**, 10690–10701.
76. Benjamin,R.C. and Gill,D.M. (1980) ADP-ribosylation in mammalian cell ghosts. Dependence of poly(ADP-ribose) synthesis on strand breakage in DNA. *J. Biol. Chem.*, **255**, 10493–10501.
77. Benjamin,R.C. and Gill,D.M. (1980) Poly(ADP-ribose) synthesis in vitro programmed by damaged DNA. A comparison of DNA molecules containing different types of strand breaks. *J. Biol. Chem.*, **255**, 10502–10508.
78. Kim,M.Y., Mauro,S., Gevry,N., Lis,J.T. and Kraus,W.L. (2004) NAD+-dependent modulation of chromatin structure and transcription by nucleosome binding properties of PARP-1. *Cell*, **119**, 803–814.
79. Langelier,M.F., Planck,J.L., Roy,S. and Pascal,J.M. (2012) Structural basis for DNA damage-dependent poly(ADP-ribosyl)ation by human PARP-1. *Science*, **336**, 728–732.
80. Dawicki-McKenna,J.M., Langelier,M.F., DeNizio,J.E., Riccio,A.A., Cao,C.D., Karch,K.R., McCauley,M., Steffen,J.D., Black,B.E. and Pascal,J.M. (2015) PARP-1 activation requires local unfolding of an autoinhibitory domain. *Mol. Cell*, **60**, 755–768.
81. Muoio,D., Laspata,N. and Fouquerel,E. (2022) Functions of ADP-ribose transferases in the maintenance of telomere integrity. *Cell. Mol. Life Sci.*, **79**, 215.
82. Chang,E.Y., Novoa,C.A., Aristizabal,M.J., Coulombe,Y., Segovia,R., Chaturvedi,R., Shen,Y., Keong,C., Tam,A.S., Jones,S.J.M. *et al.* (2017) RECQ-like helicases Sgs1 and BLM regulate R-loop-associated genome instability. *J. Cell Biol.*, **216**, 3991–4005.
83. Cristini,A., Ricci,G., Britton,S., Salimbeni,S., Huang,S.N., Marinello,J., Calsou,P., Pommier,Y., Favre,G., Capranico,G. *et al.* (2019) Dual processing of R-loops and topoisomerase I induces transcription-dependent DNA double-strand breaks. *Cell Rep.*, **28**, 3167–3181.
84. Perez-Calero,C., Bayona-Feliu,A., Xue,X., Barroso,S.I., Munoz,S., Gonzalez-Basallote,V.M., Sung,P. and Aguilera,A. (2020) UAP56/DDX39B is a major cotranscriptional RNA–DNA helicase that unwinds harmful R loops genome-wide. *Genes Dev.*, **34**, 898–912.
85. Gagne,J.P., Isabelle,M., Lo,K.S., Bourassa,S., Hendzel,M.J., Dawson,V.L., Dawson,T.M. and Poirier,G.G. (2008) Proteome-wide identification of poly(ADP-ribose) binding proteins and poly(ADP-ribose)-associated protein complexes. *Nucleic Acids Res.*, **36**, 6959–6976.
86. Gagne,J.P., Pic,E., Isabelle,M., Krietsch,J., Ethier,C., Paquet,E., Kelly,I., Boutin,M., Moon,K.M., Foster,L.J. *et al.* (2012) Quantitative proteomics profiling of the poly(ADP-ribose)-related response to genotoxic stress. *Nucleic Acids Res.*, **40**, 7788–7805.
87. Isabelle,M., Moreel,X., Gagne,J.P., Rouleau,M., Ethier,C., Gagne,P., Hendzel,M.J. and Poirier,G.G. (2010) Investigation of PARP-1, PARP-2, and PARG interactomes by affinity-purification mass spectrometry. *Proteome Sci.*, **8**, 22.
88. Larsen,S.C., Hendriks,I.A., Lyon,D., Jensen,L.J. and Nielsen,M.L. (2018) Systems-wide analysis of serine ADP-ribosylation reveals widespread occurrence and site-specific overlap with phosphorylation. *Cell Rep.*, **24**, 2493–2505.
89. Costantino,L. and Koshland,D. (2018) Genome-wide map of R-loop-induced damage reveals how a subset of R-loops contributes to genomic instability. *Mol. Cell*, **71**, 487–497.
90. Garcia-Muse,T. and Aguilera,A. (2019) R loops: from physiological to pathological roles. *Cell*, **179**, 604–618.
91. Rinaldi,C., Pizzul,P., Longhese,M.P. and Bonetti,D. (2020) Sensing R-loop-associated DNA damage to safeguard genome stability. *Front. Cell Dev. Biol.*, **8**, 618157.
92. Sollier,J., Stork,C.T., Garcia-Rubio,M.L., Paulsen,R.D., Aguilera,A. and Cimprich,K.A. (2014) Transcription-coupled nucleotide excision repair factors promote R-loop-induced genome instability. *Mol. Cell*, **56**, 777–785.
93. Freudenreich,C.H. (2018) R-loops: targets for nuclease cleavage and repeat instability. *Curr. Genet.*, **64**, 789–794.
94. Illuzzi,G., Fouquerel,E., Ame,J.C., Noll,A., Rehmet,K., Nasheuer,H.P., Dantzer,F. and Schreiber,V. (2014) PARG is dispensable for recovery from transient replicative stress but required to prevent detrimental accumulation of poly(ADP-ribose) upon prolonged replicative stress. *Nucleic Acids Res.*, **42**, 7776–7792.
95. Cortez,D. (2015) Preventing replication fork collapse to maintain genome integrity. *DNA Repair (Amst.)*, **32**, 149–157.
96. Haince,J.F., McDonald,D., Rodrigue,A., Dery,U., Masson,J.Y., Hendzel,M.J. and Poirier,G.G. (2008) PARP1-dependent kinetics of recruitment of MRE11 and NBS1 proteins to multiple DNA damage sites. *J. Biol. Chem.*, **283**, 1197–1208.

97. Groh,M. and Gromak,N. (2014) Out of balance: r-loops in human disease. *PLos Genet.*, **10**, e1004630.
98. Ye,B.J., Kang,H.J., Lee-Kwon,W., Kwon,H.M. and Choi,S.Y. (2021) PARP1-mediated PARylation of TonEBP prevents R-loop-associated DNA damage. *DNA Repair (Amst.)*, **104**, 103132.
99. Altmeyer,M., Neelsen,K.J., Teloni,F., Pozdnyakova,I., Pellegrino,S., Grofte,M., Rask,M.D., Streicher,W., Jungmichel,S., Nielsen,M.L. *et al.* (2015) Liquid demixing of intrinsically disordered proteins is seeded by poly(ADP-ribose). *Nat. Commun.*, **6**, 8088.
100. Dettori,L.G., Torrejon,D., Chakraborty,A., Dutta,A., Mohamed,M., Papp,C., Kuznetsov,V.A., Sung,P., Feng,W. and Bah,A. (2021) A tale of loops and tails: the role of intrinsically disordered protein regions in R-loop recognition and phase separation. *Front. Mol. Biosci.*, **8**, 691694.